High-resolution angle- and energy-resolved photoelectron spectroscopy of NO: Partial wave decomposition of the ionization continuum

Sarah W. Allendorf,[a] David J. Leahy, Dennis C. Jacobs,[b] and Richard N. Zare
Department of Chemistry, Stanford University, Stanford, California 94305

(Received 23 February 1989; accepted 5 May 1989)

We report a two-color high-resolution energy- and angle-resolved study of the photoelectrons produced in the $(1 + 1')$ REMPI of NO via rotational levels of the $A\ ^2\Sigma^+$ $v = 0$ state. We find markedly different photoelectron angular distributions arising from production of ions in different rotational states ($\Delta N = 0, \pm 1, \pm 2$ transitions in the ionization step). We also observe that the $\Delta N = \pm 2$ angular distributions are very sensitive to the intermediate state alignment. A model is put forward in which experimental observables (angle- and energy-resolved photoelectron spectra) are used to determine the attributes (relative amplitudes and phase shifts) of a small number of interfering continuum channels that contribute to the ionization step as well as the fraction of parallel character of the ionization step. Nearly 70% of the ejected photoelectrons are associated with the $\Delta N = 0$ ionization transition; the partial wave composition of these electrons is dominated by p character. The less important $\Delta N = \pm 1$ peaks have both s- and d-wave character. The $\Delta N = \pm 2$ photoelectron peaks exhibit far more f-wave than p-wave character because destructive interference nearly removes the p-wave contribution to the angular distribution. The partial wave decomposition is used to predict angular distributions resulting from excitation of the intermediate state by different rotational branch transitions; these predictions are in excellent agreement with the measured distributions.

I. INTRODUCTION

Photoelectron spectroscopy (PES) continues to be an attractive technique for the study of photoionization dynamics.[1,2] Because the ejected photoelectron is so much lighter than the parent ion, it carries much of the dynamical information about the photoionization process. The photoelectron energy distribution reflects the energy deposited in the accompanying ion. For molecular ions this information is tantamount to obtaining an infrared spectrum, that is, it allows the identificaiton of different vibrational levels excited in the ion. The angular distribution of the photoelectron also carries much information.[1-5] It has been used as a measure of the anisotropy in the photoionization process and as a signature for such phenomena as autoionization and shape resonances.[5] In the case of single-photon ionization from an isotropic ensemble of atoms or molecules, the measured distribution is commonly described as[6]

$$I(\theta) = 1 + \beta_2 P_2(\cos\theta), \tag{1}$$

where $P_2(\cos\theta) = \frac{1}{2}(3\cos^2\theta - 1)$ is the second Legendre polynomial, θ is the angle between the electric field vector of the incident light beam (assumed to be linearly polarized) and the detection axis, and β_2 is known as the asymmetry parameter. In the case of atomic photoionization, β_2 is a signature of the partial wave composition as well as the interference (differential phase shift) of the outgoing partial waves at the chosen photoelectron energy.[7]

In recent years, resonance enhanced multiphoton ionization (REMPI) has added an extra dimension to the study of the photoionization process.[8,9] An $(n + m)$ REMPI event can be viewed[10] as a two-step process with an n-photon absorption from the ground state to the resonant intermediate state, followed by an m-photon absorption from the intermediate state to the ionization continuum. An $(n + 1)$ REMPI process simplifies the ionization dynamics by removing interferences of virtual and real states between the resonant and continuum states. Moreover, $(n + 1)$ REMPI brings to the study of photoionization dynamics of molecules the ability to probe ionization from a specific quantum state. This ability eliminates the need to deconvolute the contributions from the thermal population distribution in the initial ground state, which must be included in single-photon photoionization. Additionally, a multiple-photon technique can expose more of the anisotropy present in the system. For example, the angular distribution for an $(n + m)$ REMPI process has the general form

$$I(\theta) = \sum_{L=0}^{L_{\max}/2} \beta_{2L} P_{2L}(\cos\theta), \tag{2}$$

where $P_L(\cos\theta)$ is the L th Legendre polynomial, and the upper limit on the summation depends on both the molecular properties and the dynamics of the REMPI process itself. In the limit where no saturation occurs, $L_{\max} = 2(n + m)$.[10] Finally, it is worth emphasizing that the REMPI process has greatly expanded the number of molecular systems whose photoionization dynamics can be conveniently probed because of the ability to use more than a single photon to reach the ionization continuum.

Recently, several experimental techniques have emerged as the techniques of choice for REMPI-PES. The

[a] Present address: Lawrence Livermore National Laboratory, L-483, P. O. B. 808, Livermore, CA 94551.
[b] Present address: Department of Chemistry, University of Notre Dame, Notre Dame, IN 46556.

 0021-9606/89/162216-19$02.10

highest energy resolution has been achieved using the zero-kinetic energy photoelectron technique (the "ZEKE" method), pioneered in the group of Schlag and co-workers.[11] Their reported resolution, $< 1.2\,\mathrm{cm}^{-1}$ (0.15 meV), is unprecedented in the field of PES, and is limited more by the laser systems employed than by the difficulties of working with photoelectrons! The ZEKE method is well suited to the study of photoionization at the energetic threshold, but appears so far to be of limited usefulness for measuring the anisotropy of the angular distribution of the photoelectrons because the near threshold photoelectrons are so easily distorted by stray fields. An alternative detection technique gaining popularity with the PES community utilizes the "magnetic bottle" apparatus, developed by Kruit and Read.[12] This apparatus has the advantages of 2π-steradian collection (enhancing the signal-to-background of PES experiments) and excellent energy resolution (about 20 meV for 1 eV photoelectrons). The "magnetic bottle" unfortunately lacks angular resolution because of its collection method. Because of the shortcomings of the ZEKE and magnetic bottle techniques, we have chosen the more traditional PES technique of time of flight (TOF). This allows measurement of doubly differential photoelectron scattering distributions, that is, simultaneously angle- and energy-resolved photoelectron spectra. Sufficient angular resolution is facile in a field-free TOF experiment; energy resolution, while more difficult, is aided by choosing a photoelectron energy sufficiently low to provide the necessary resolution but high enough for the photoelectron's trajectory to be relatively free from disturbing static fields.

The first atomic angle-resolved REMPI-PES study was performed in 1974 by Berry and co-workers,[13] who ionized titanium atoms in a resonant two-photon process. The technique of REMPI-PES angular distributions appears to have first been extended to molecules by Achiba *et al.*[14] They recorded the angular distributions resulting from $(3+1)$ REMPI of both NO and NH_3. Since then, investigators have extended this work to different electronic states of NO,[15–20] as well as to other molecules, for example, H_2[21,22] and O_2.[23] In almost all of these cases the apparatus used did not have sufficient energy resolution to associate the outgoing photoelectron with a unique rotational state of the molecular ion. An important exception was the pioneering study by Reilly and co-workers,[18,24] who investigated $(1+1)$ REMPI of NO via the $A\,^2\Sigma^+$,$C\,^2\Pi$, and $D\,^2\Sigma^+$ excited states. They were able to obtain partial resolution of the photoelectrons arising from production of ions in different rotational states ("rotational resolution"). With their laser tuned to a specific rotational transition between the ground state and the excited state, the photoelectron energy distribution was observed to change markedly when the direction of the linear polarization of the laser was varied from parallel to perpendicular with respect to the detection direction. This work encouraged a number of *ab initio* calculations.[25–28]

In this paper we report an extension of the study of Reilly and co-workers on the (0,0) band of the NO $A\,^2\Sigma^+$–$X\,^2\Pi$ transition. We are able to achieve complete rotational resolution of the photoelectrons in a slightly different region of the ionization continuum by using a two-color REMPI scheme, which we call $(1+1')$ REMPI. We find that photoelectron angular distributions measured under these rotationally resolved conditions are strongly dependent on the change in rotational angular momentum in the photoionization transition; i.e., photoelectron peaks that correspond to the production of ions with different amounts of rotational energy have very different angular distributions. Dynamical information about the relative amplitudes and phase shifts of the outgoing photoelectron waves as well as the symmetry nature of the photoionization transition can be extracted from these energy- and angle-resolved spectra. We present a model that parametrizes the measured distributions in terms of the amplitudes and relative phase shifts of a small number of interfering partial waves contributing to the photoionization process. The results of this model permit a direct comparison with *ab initio* calculations on this system.[29]

II. EXPERIMENTAL

The ability to achieve rotational resolution in our TOF apparatus requires a careful experimental strategy. High-resolution PES of NO is aided by production of ions in relatively high rotational levels where the rotational spacing is large enough to be resolved with a nonthreshold photoelectron technique. Additionally, we have selected a two-color scheme to provide photoelectrons with low kinetic energy, taking full advantage of our TOF apparatus. This, in turn, makes our experiment very sensitive to the physical environment of the flight tube.

There are a number of experimental factors that broaden a TOF peak. Lower-energy photoelectrons are much more susceptible to stray fields, both magnetic and electric, that easily distort their trajectories. The major source of magnetic fields is the earth itself, but fields from the turbomolecular pumps used to evacuate our chamber contribute as well. More difficult to eliminate are electric fields. We introduce some of these fields (i.e., the high-voltage fields applied to the CEMA detector, and Coulomb broadening from production of too many charged particles in a limited space), but most arise from surface potentials developed on charged adsorbed layers at the walls of the vacuum chamber. Other causes of peak broadening are related to the nonideal conditions of our experiment. For example, laser ionization does not produce a perfect point source of electrons, so different electrons travel different distances to the detector. This difference, δL, is insignificant compared to the mean distance, L. Additionally, use of a 6 ns pulsed laser imposes an ultimate resolution of 6 ns wide peaks. Although peaks arising from faster electrons are observed to be limited by this laser pulse width, the slower electrons studied here arrive during a wider time interval (15–20 ns) than the laser pulse width. The electronics with which we detect the photoelectron arrival events may introduce artificial broadening to the measured TOF peaks; this is best avoided through use of pulse-counting techniques that associate a single flight time with each electron arrival event. Thus, the most serious limitation on achieving high photoelectron energy resolution is the nonuniformity (both spatial and temporal) of fields inside the flight tube. This causes photoelectrons

whose trajectories are slightly different to experience different potentials, and thus to be accelerated or slowed to different extents. In what follows we describe our apparatus, specifically addressing these concerns.

Modifications to the previously reported time-of-flight photoelectron spectrometer[21,30] include increased pumping capabilities and the addition of a source chamber, which allows skimming of the molecular beam. Figure 1 is a schematic drawing of the experimental setup. The apparatus consists of two chambers. Each is pumped by a turbomolecular pump backed by a mechanical pump. The background pressure in the main chamber is 7×10^{-9} Torr; that of the source chamber is 1×10^{-8} Torr. The source chamber contains a heatable pulsed nozzle (General Valve) and is separated from the ionization/detection chamber by a 0.3 mm skimmer (Beam Dynamics). The output of the skimmed molecular beam is crossed at right angles by the two counterpropagating laser beams. Those photoelectrons ejected in the direction mutually orthogonal to the laser beams and the molecular beam travel 51 cm to a CEMA detector (Galileo Optics FTD-2003). The importance of a double-mesh ground shield placed directly in front of the CEMA was demonstrated by modeling the photoelectron trajectories in our "field-free" apparatus.[31] This modeling indicated significant field leakage when no ground shields were in place because of the small field applied to the front plate of the CEMA. Our 5 cm diameter detector collects photoelectrons ejected into a solid angle of $\pm 3°$. This corresponds to the detection of approximately 6 out of 10 000 photoelectrons (assuming an isotropic distribution).

The output of the CEMA passes thorough a fast preamplifier and then into one of three instruments: a boxcar (SRS 275) for wavelength scanning, a fast transient digitizer (Tektronix 7912AD) for relatively low signal levels (5–10 photoelectron arrivals per laser shot), or a time-to-pulse-height converter (TPHC) (EG&G Ortec 450) for very low signal levels (less than 1 photoelectron arrival per 10 laser shots). Coulomb broadening of measured peaks is readily observed when detected signals are above a rate of 2 photoelectron arrivals per laser shot, corresponding to production of about 4000 photoion/photoelectron pairs. Laser power and focusing conditions were selected to maintain the maximum signal level of approximately 1 photoelectron every 10 laser shots for the high-resolution photoelectron spectra presented here. An IBM PC/XT interfaces with the transient digitizer, boxcar, and TPHC; the data presented here were all recorded using the TPHC, with multichannel analysis, storage, and processing performed by the PC/XT running in the ASYST (Asyst Software Technologies) operating environment.

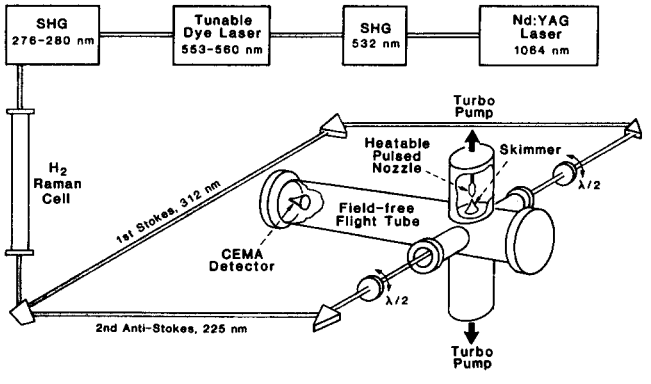

FIG. 1. Schematic diagram for REMPI-PES showing the vacuum chamber and the production of tunable, two-color UV radiation.

The flight tube consists of two concentric mu-metal tubes (AdVance Magnetics, Inc.) with 0.025 in. walls held in place by stainless steel spacers. We initially electroplated the innermost surface with gold. After a bake (200 °C for several days) to remove trapped water, we observed 6 meV resolution at a photoelectron energy of 180 meV. However, subsequent occasional but necessary venting of the apparatus led to inconsistent resolution. Our best success was achieved by overcoating the gold-plated flight tube with colloidal graphite (Aerodag, Acheson Colloids). Great care was taken to coat the surface thoroughly, using UHV techniques such as powderless gloves to keep skin oils from contacting the clean surface. The best results were observed when the flight tube was freshly cleaned with isopropyl alcohol and resprayed with colloidal graphite after each venting of the chamber; then the chamber was evacuated and baked at 150 °C for at least 72 h. With this protocol we were able to achieve reproducibly a resolution on the order of 2 meV FWHM at a photoelectron energy of 180 meV.

Flight times are very sensitive to changing contact potentials in the flight tube because of the low energy of the photoelectrons. An incremental increase on the order of 10 ns per day was observed in the peak positions as the environment of the flight tube became contaminated. Baking to 150 °C improved the cleanliness of the flight tube somewhat, but flight times never returned to the times observed in a freshly cleaned apparatus. The most reliable solution to flight-tube contamination is to vent, clean, and respray the tube. Broadening of the peaks (and degradation of the resolution) was observed to occur over usually three to four weeks. For these reasons, no attempt was made to calibrate the spectrometer.

Tunable UV radiation at 225 nm is required for the first step of this (1 + 1′) REMPI process while light at 312 nm effects the ionization. These two colors are generated in the following manner: a frequency-doubled Nd:YAG laser (Quanta-Ray DCR-1) pumps a dye laser (Quanta-Ray PDL-1), the output of which is frequency doubled (WEX-1), then focused (50 cm focal length) in the center of a hydrogen-filled cell where Raman shifting occurs. After recollimation the second anti-Stokes and first Stokes orders are separated and directed to opposite sides of the ionization chamber. After the last turning prism and just prior to entering the chamber, each laser beam passes through a Glan–Taylor prism polarizer (Karl Lambrecht) and a zero-order half-waveplate (Special Optics, centered at 225 or 312 nm) mounted in a computer-controlled precision rotation mount. In both cases the degree of linear polarization is greater than 99%. The two colors enter the apparatus simultaneously (within 0.3 ns).

The spectrum of the NO $A\,^2\Sigma^+$–$X\,^2\Pi$ transition is well known.[32,33] Ionization with 312 nm rather than 225 nm light

does not affect the relative REMPI spectral intensities. We utilize the R_{21} (20.5) and $Q_{11}+P_{21}$ (25.5) resonant transitions for the experiments described here. The dynamics of the REMPI process have been shown to be very sensitive to laser power.[28,33,34] A spatially homogeneous portion of the second anti-Stokes beam is selected with an iris diaphragm prior to focusing. The pulse energy of this 1 mm diameter beam is on the order of 1–2 μJ per pulse. We focus this radiation mildly with a 50 cm focal length lens positioned so that its focal point is approximately 3 cm past the intersection with the molecular beam. Careful alignment is critical in order to minimize background photoelectrons resulting from stray 225 nm photons. Background photoelectrons from the 312 nm light are not a serious problem and are reduced by directing this light through the chamber slightly off axis. This radiation is also mildly focused with a 50 cm focal length lens whose focal point is approximately 3 cm past the laser–molecular beam intersection. Prior to focusing, the energy in the 1 cm diameter first Stokes beam is on the order of 400 μJ per pulse.

Nitric oxide (Matheson 99.0%) is admitted to the ionization chamber through the skimmed pulsed nozzle with 3 PSI backing pressure, the minimum pressure that can be reliably regulated. Because we access such a high rotational level of the ground state, we want to minimize rotational cooling in the nozzle expansion. A home-built resistive-heating element shrouds the nozzle and heats it to 65 °C. A 0.8 mm nozzle orifice is used, which serves to increase the nozzle throughput. From the ionization signal as a function of wavelength, we estimate an approximate rotational temperature of 225 K, with population observable in ground state rotational levels as high as $J_g = 25.5$. The pressure in the source chamber during nozzle operation is typically 6×10^{-5} Torr, leading to an ionization chamber pressure of 1×10^{-7} Torr during experiments.

Photoelectron energy spectra presented here were accumulated during 15 000 laser shots with a delayed 1.0 μs gate on the TPHC. During 90% of these laser shots no photoelectrons arrived at the detector, i.e., neither signal nor background photoelectrons were observed. The rotational assignments in the spectra are based on a one-time calibration of the TOF spectrometer using all of the Raman orders from the Raman shifter to produce ionization. Several spectra taken that same day were inverted from time to energy. This inversion is based on this calibration, the known ionization potential of NO,[35] and the known NO^+ X state molecular constants.[36] The peaks in the TPHC spectra were assigned as arising from a progression in rotational levels in the ion, centered around $\Delta N = 0$. The TPHC spectra presented here have not been converted to energy because of changing contact potentials in the flight tube over the course of several weeks.

Angular distributions were recorded by the following procedure. For each run, TOF photoelectron spectra were obtained for ten different angles θ, where θ is the angle between the electric field vector of the ionization laser and the detection axis. This was done twice, with the angle χ (the angle between the electric field vectors of the two laser beams) set equal to 0° or 90°, so that each run consisted of 20 (χ,θ) pairs. At each (χ,θ) position of the waveplates, we accumulated signal for 750 laser shots, during which the output of the TPHC was binned into one of the 20 signal arrays. We jumped from angle to angle in order to minimize the effects of long-term drift in the pulse power and wavelength of the laser system. The set of 20 (χ,θ) pairs was repeated 10 times, for a total of 7500 laser shots per step. Such an experiment, lasting about 4 h, was repeated on several days. The measured angular distributions were reproducible from experiment to experiment, taking into account the poor statistics of only 7500 laser shots per (χ,θ) pair. In each experiment, the signal corresponding to different ΔN peaks was integrated separately. The integrations of several experiments were then combined to give the data presented here, indicated in the plots of the angular distributions as filled circles. Ten values of θ were measured in only one quadrant. Preliminary work confirmed the expected symmetry of the four quadrants in our experimental apparatus.

III. RESULTS

A. Two-color photoelectron energy spectra

We are studying the multiphoton ionization of NO via the (0,0) band of the $A\,^2\Sigma^+$–$X\,^2\Pi$ transition, specifically via the R_{21} (20.5) and $Q_{11}+P_{21}$ (25.5) resonant transitions. The relevant energetics are shown in Fig. 2. We use a two-color (1 + 1′) REMPI scheme in which 225 nm light provides the energy for the resonant step and 312 nm radiation induces the ionization from the intermediate state. The latter color is of insufficient energy to excite ground state NO mol-

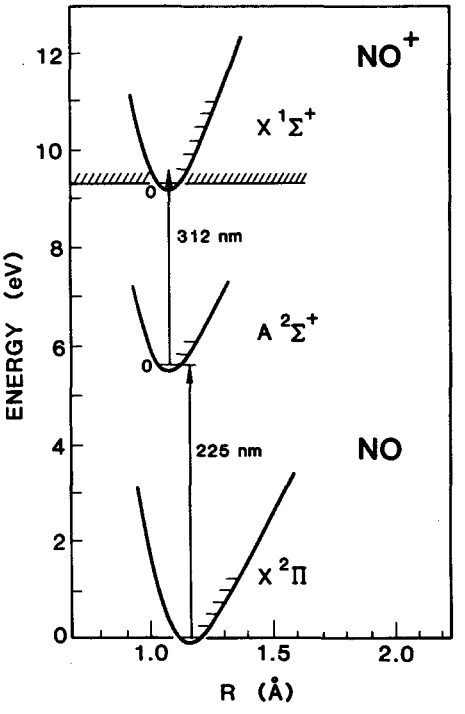

FIG. 2. Energy level diagram for (1 + 1′) REMPI of NO. Only the relevant energy states are shown. Also indicated are the resonant photon (225 nm) and the ionization photon (312 nm).

ecules. Single-color REMPI by the 225 nm light produces relatively fast photoelectrons with an energy near 1.7 eV, as well as very low energy electrons arising from autoionization processes.[37] Fast photoelectrons are observed under increased laser power or tighter focusing conditions but are not observed under the conditions used for this work. Slow photoelectrons are not detected under the field-free conditions employed in this experiment but can be observed with the use of an extraction field. The ionization energy provided by the first Stokes radiation (312 nm) is sufficient to populate only $v^+ = 0$ in the ion, leaving approximately 180 meV of energy for the photoelectrons produced in a $\Delta N = 0$ ionization transition.

Figure 3(a) shows a typical two-color photoelectron energy spectrum produced by REMPI-PES via the R_{21} (20.5) line of the NO $A\,^2\Sigma^+$–$X\,^2\Pi$ transition. This spectrum is recorded with the polarization of both lasers parallel to the detection axis. The five base line-resolved PES peaks correspond to production of ions in five different rotational levels. Each peak carries a satellite peak occurring at later time; the most prominent of these is that of the central peak. We assign the $\Delta N = 0$ photoionization transition as the source of the photoelectrons in this satellite peak because the ratio of the central peak to its satellite is independent of nozzle temperature, intermediate state rotational level, and the photoelectron energy of the central peak. Variation in the intensities of the lasers as well as in the delay between them also has no effect on the ratio of their areas. However, from vent to vent the relative areas of the two peaks do change, indicating that the satellite peak is an artifact of the cleanliness of the apparatus. Early in our investigations there was no satellite observable under conditions of nearly the same resolution (6 meV FWHM for photoelectrons at 180 meV). The polarization behavior of the satellite peak is observed to track that of the central peak. Time-of-flight measurements accumulated over 50 000 laser shots show that each of the $\Delta N \neq 0$ peaks also has a satellite peak at later time. Under the conditions reported here, the satellite peaks for the $\Delta N \neq 0$ photoelectron peaks were sufficiently small to be neglected. The satellite peak of the central $\Delta N = 0$ peak was not included in the integration of the TPHC spectra.

Each PES peak is labeled with the respective change in the rotational quantum number of the corresponding ion. The peaks in Fig. 3(a) demonstrate that $\Delta N = 0, \pm 1$, and ± 2 photoionization transitions occur in this sytem, with a somewhat less clear indication of $\Delta N = \pm 3$ transitions. At this polarization, with the electric field vector of both lasers parallel to the detection axis, the TOF spectrum is dominated by the $\Delta N = 0$ photoelectron peak.

B. Intermediate state alignment

The use of a linearly polarized laser for excitation from an isotropic ground state creates an aligned intermediate state. The total angular momentum $\mathbf{J}_1$ of the intermediate state makes the projection M_J on the space-fixed Z axis, which we choose to be the polarization vector of the ionization laser beam. A sample is said to be aligned when states with high $|M_J|$ are more populated than those with low $|M_J|$, or vice versa; a sample is said to be isotropic if all the M_J sublevels are equally populated. There are two ways to vary the alignment of the excited state. First, we can rotate the plane of polarization of the excitation laser while keeping the ionization laser's polarization fixed relative to the detection axis. In such an experiment, rotating the polarization of the excitation laser with respect to that of the ionization laser prepares a different intermediate state alignment prior to ionization. The spectrum in Fig. 3(b) is taken under conditions identical to those of Fig. 3(a) except that the excitation laser polarization is perpendicular to the detection axis. The effect of the intermediate state alignment on the relative importance of photoelectrons produced by $\Delta N \neq 0$ photoionization transitions is pronounced.

A second way to vary the alignment of the intermediate state is to excite a different branch of the resonant transition. The probability for an optical transition is proportional to $|\langle \boldsymbol{\mu} \cdot \mathbf{E} \rangle|^2$, where $\boldsymbol{\mu}$ is the transition dipole moment and $\mathbf{E}$ is the polarization vector. For a linear molecule, $\boldsymbol{\mu}$ is in the

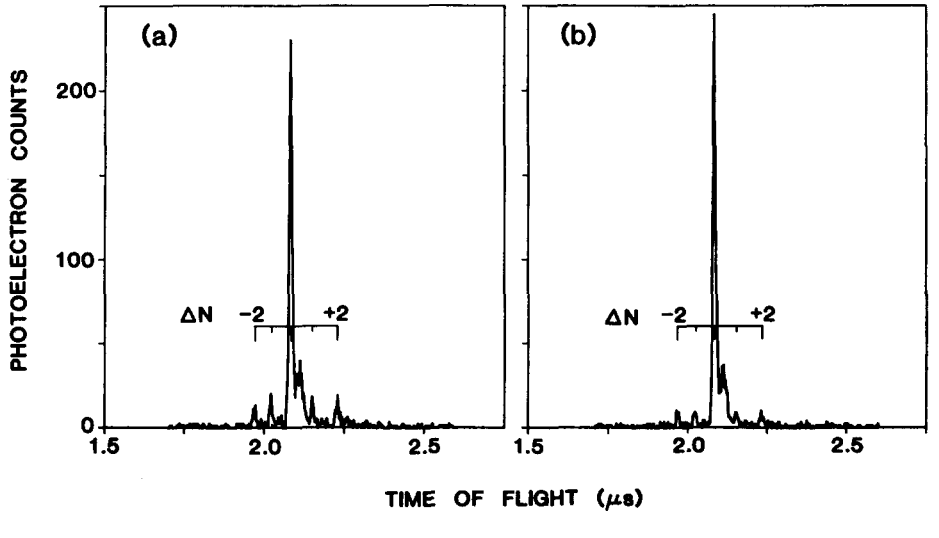

FIG. 3. Two-color time-of-flight photoelectron spectra via the NO A–$X\,R_{21}$ (20.5) resonant excitation. The electric field vector of the resonant laser is (a) parallel or (b) perpendicular to the detection axis. In both cases the electric field vector of the ionization laser is parallel to the detection axis. Each peak is labeled with ΔN, the change in rotational angular momentum in the ionization transition. Not labeled are satellite peaks (see the text).

plane of rotation for an R or P branch ($\Delta J = \pm 1$) in the classical limit. It can be shown[34] that an R or P branch produces a population that peaks at $M_J = 0$ (i.e., $\mathbf{J}\cdot\mathbf{E} = 0$) and is minimal at $M_J = \pm J$. For a Q branch ($\Delta J = 0$), μ is along $\mathbf{J}$ in the classical limit. Thus, the opposite alignment is predicted (peaking at $M_J = \pm J$ and minimal for $M_J = 0$). Figure 3 applies to the R_{21} (20.5) branch transition that is a "pure" rotational line. There are no rotationally pure Q branch transitions because of the unresolved spin–rotation splitting in the $A\,^2\Sigma^+$ state. However, the $Q_{11} + P_{21}$ (25.5) line is predominantly Q in character. We calculate that the Q:P ratio is 8:1 based on relative rotational line strengths.[38,39]

Figures 4(a) and 4(b) present the photoelectron energy distribution for REMPI via the $Q_{11} + P_{21}$ (25.5) transition, with the resonant laser polarized parallel and perpendicular to the detection axis, respectively. In both, the electric field vector of the ionization laser is parallel to the detection axis. Figure 4(a) is similar to what is observed when the R branch is probed at 90° [Fig. 3(b)], while Fig. 4(b) is similar to Fig. 3(a). It is inaccurate to compare the absolute intensity differences between Figs. 3 and 4 because of beam walk associated with the wavelength change and because of uncertainties in the relative population of the two ground states. However, it is valid to compare the relative importance of the $\Delta N \neq 0$ peaks in these two figures. The effect of the alignment of the intermediate state, while not large, is evident. The relative ΔN populations depend on the intermediate state alignment. It must be stressed Figs. 3 and 4 present data for photoelectrons ejected in only one direction. It is necessary to measure the full angular distributions to obtain a more nearly complete picture of the effect of intermediate state alignment.

C. Angular distributions

Previous investigators have measured single-color molecular REMPI-PES angular distributions by rotating the polarization of "both" lasers together, in the spirit of single-photon angular distributions.[14–24] Our goal is to separate the photoionization step from the resonant excitation step in order to understand the dynamics of the photoionization process itself. The use of polarization for this purpose has been employed by several investigators of atomic REMPI-PES angular distributions.[40] We also choose to use a pump–probe scheme in which we prepare the intermediate state alignment with the first laser beam, then probe the alignment by measuring the photoelectron angular distribution with the second laser beam. We vary the alignment of the excited state by changing the polarization rather than by exciting different branch transitions (R vs Q) for the reasons mentioned in Sec. III B. This allows comparison of absolute intensities recorded during a single experiment.

Figures 5(a) and 5(b) present the photoelectron angular distributions from the R_{21} (20.5) resonant transition with the polarizations of the two lasers parallel and perpendicular to each other, respectively. The angular distributions are labeled with the change in rotational quantum number for the photoionization transition. These distributions are presented as polar plots, where the angle is that between the electric field vector of the ionization laser and the detection axis, and the radius is the integrated intensity of the photoelectron peak measured at that angle. The detection axis is in the vertical direction for all polar plots. The angular distributions from top to bottom in each figure are plotted in the order in which they occur in the TOF spectrum, i.e., the earliest peak (highest-energy photoelectrons) is at the top of the column. Because of the relationship of flight time to energy, integration for the peaks following the $\Delta N = 0$ peak was done over more bins than for the earlier peaks. Additionally, Coulomb broadening causes some of the more numerous $\Delta N = 0$ photoelectrons to arrive late, thus distorting the angular distributions for the $\Delta N = +1$ and $\Delta N = +2$ peaks. Consequently, the distributions are less reliable on the late side of the large $\Delta N = 0$ peak.

The dashed curves are drawn based on a separate fit of the raw data of each angular distribution to the customary zeroth, second, and fourth Legendre polynomials [Eq. (2)]. The resulting β_i coefficients, along with the correlation coefficient r for each fit, are listed in Table I(A). For the pur-

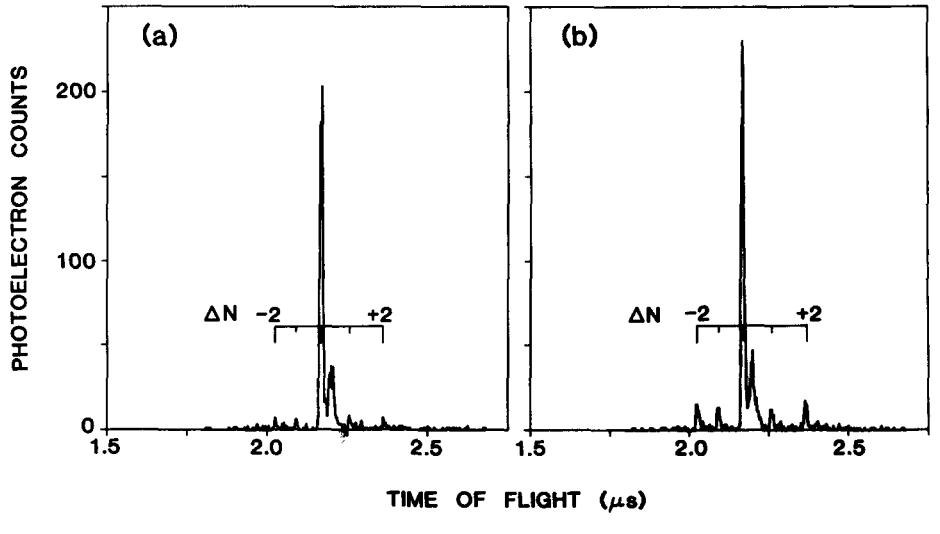

FIG. 4. Two-color time-of-flight photoelectron spectra via the NO A–X $Q_{11} + P_{21}$ (25.5) resonant excitation. The electric field vector of the resonant laser is (a) parallel or (b) perpendicular to the detection axis. In both cases the electric field vector of the ionization laser is parallel to the detection axis. Each peak is labeled with ΔN, the change in rotational angular momentum in the ionization transition. Not labeled are satellite peaks (see the text).

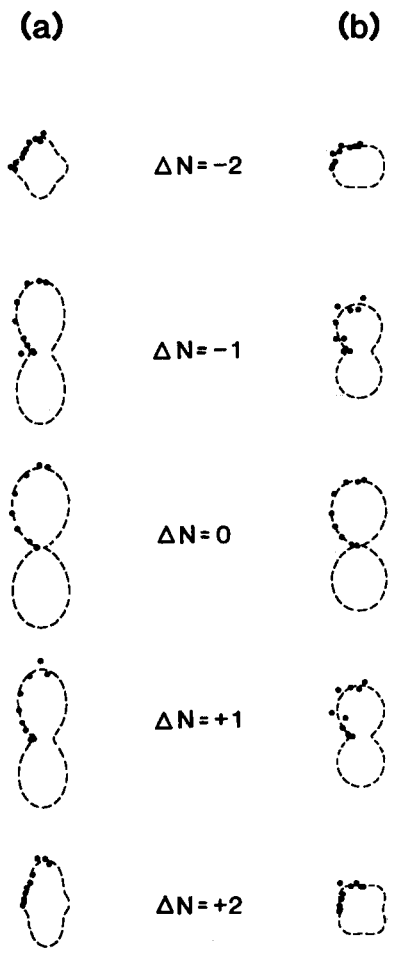

FIG. 5. Polar plots of the two-color photoelectron angular distributions for the five rotational peaks in Fig. 3. Excitation is via the R_{21} (20.5) transition. In (a) the electric field vectors of the two lasers are parallel to each other ($\chi = 0°$), while in (b) the electric field vector of the resonant laser is perpendicular to the electric vector of the ionization laser ($\chi = 90°$). The dashed curves represent a fit of the data to Legendre polynomials as discussed in the text (see Table I); the solid circles are the measured data. In all cases, $\beta_0 \equiv 1.000$.

pose of presenting the angular distributions, we set $\beta_0 \equiv 1.000$ and normalize each raw data set accordingly. It is interesting to note the relative importance of the $\Delta N \neq 0$ photoionization channels, as evidenced by the relative values of β_0 listed in Table I(A). The decrease of $\Delta N \neq 0$ contributions with increasing $\mathbf{J}_1$, as observed (at low values of $\mathbf{J}_1$) by Sander *et al.*,[11] is clearly not present here. This discrepancy has been discussed by Rudolph, McKoy, and Dixit.[41] They argue that this result arises from observing P_{11} branch transitions at low values of $\mathbf{J}_1$.

The most obvious feature of Fig. 5 is the dependence of the angular distributions on the change in rotational quantum number ΔN. This dependence was also observed for photoionization via a different intermediate J_1. What is important is not the final J^+ state but rather the change in J during the photoionization process. Therefore, we expect that the photoelectron angular distributions for a given $|\Delta N|$ would be similar. This similarity is observed in Fig. 5(a) between the $\Delta N = -1$ and $\Delta N = +1$ photoelectron angular distributions, but is seen to a lesser degree for $\Delta N = -2$ compared to $\Delta N = +2$. This asymmetry of the $|\Delta N| = 2$ is not so severe when the opposite alignment of the intermediate state is prepared, as can be seen in Fig. 5(b). These angular distributions were reproduced a number of times, and we are presently unable to account for this anomaly.

Because the $\Delta N = 0$ peak is so much larger than the $\Delta N \neq 0$ peaks, its shape would be expected to dominate a rotationally averaged angular distribution. Figure 6 shows the effect of averaging each set of angular distributions in Fig. 5 weighted by the angle-integrated intensity β_0 of each

TABLE I. R_{21} (20.5) excitation: angular distributions fit to Legendre polynomials.

		$\Delta N = -2$	$\Delta N = -1$	$\Delta N = 0$	$\Delta N = +1$	$\Delta N = +2$
(A) Raw data						
$\chi = 0°$	β_0	64.594	28.791	428.664	36.957	70.127
	β_2	0.004	1.446	1.965	1.421	0.399
	β_4	0.249	0.418	0.248	0.356	0.315
	r	0.783	0.991	0.998	0.990	0.971
$\chi = 90°$	β_0	62.560	30.936	553.678	42.321	75.391
	β_2	−0.085	0.957	1.718	1.109	0.168
	β_4	−0.087	−0.073	−0.098	−0.059	−0.214
	r	0.755	0.940	0.999	0.945	0.729
(B) Calculated values based on fit to model with R_{21} (20.5) excitation data						
$\chi = 0°$	β_0	74.091	44.092	491.896	45.225	77.314
	β_2	0.228	0.793	1.826	0.786	0.200
	β_4	−0.007	0.231	−0.002	0.206	−0.013
$\chi = 90°$	β_0	63.395	45.538	506.234	47.672	69.968
	β_2	0.180	0.744	1.799	0.748	0.196
	β_4	0.004	−0.112	0.001	−0.098	0.007
(C) Prediction based on fit to model with $Q_{11} + P_{21}$ (25.5) excitation data						
$\chi = 0°$	β_0	57.113	45.774	654.282	46.773	60.659
	β_2	0.171	1.326	1.893	1.324	0.157
	β_4	0.182	0.057	−0.011	0.052	0.162
$\chi = 90°$	β_0	52.952	35.187	659.931	37.011	57.829
	β_2	0.158	1.290	1.884	1.291	0.165
	β_4	−0.098	−0.037	0.005	−0.033	−0.085

rotational peak. This angular distribution is similar to that reported by a number of investigators for photoionization from the $A\,^2\Sigma^+$ ($v = 0$) state.[19] Comparison of Figs. 5 and 6 shows a striking loss of information when the rotational state of the ion is not distinguished.

An additional feature of Fig. 5 is the effect of the intermediate state alignment. Comparison of Fig. 5(a) with Fig. 5(b) shows that the ΔN peaks have different angular distributions for different intermediate states, especially the $\Delta N = \pm 2$ peaks. This sensitivity to the intermediate state alignment decreases when the final rotational state of the ion is not resolved (see Fig. 6). This may explain why Appling *et al.*[19] were unable to observe the effect of the intermediate state alignment on their photoelectron angular distributions.

We also measured the REMPI-PES angular distribution for excitation via the NO A–X $Q_{11} + P_{21}$ (25.5) line. These distributions are presented in Figs. 7(a) and 7(b); the values of β_i obtained by fitting to Eq. (2) are presented in Table II(A). Again, the effect of the intermediate state alignment is obvious. As expected from the TPHC spectra in Figs. 3 and 4, Fig. 7(a) resembles Fig. 5(b), while Fig. 7(b) resembles Fig. 5(a). Once again, the loss of information is marked when the final state of the ion is not rotationally resolved. This is demonstrated in Figs. 6(c) and 6(d), which are analogs of Figs. 6(a) and 6(b) for the $Q_{11} + P_{21}$ (25.5) excitation.

In Fig. 8 we present the angular distributions measured via the R_{21} (20.5) resonant transition, with 54.7° between the laser polarizations (the so-called magic angle). In this figure each distribution has been fit to two curves: first, an expression involving the zeroth, second, and fourth Legendre polynomials (dotted curve); and second, an expression involving only the zeroth and the second Legendre polynomials (dashed curve), as appropriate for photoionization from a completely isotropic state. We conclude that under these conditions, the state from which ionization occurs is completely isotropic. This result is as expected; we carried out this study as a further check that the variation in our angular distributions with the relative laser polarizations was free from systematic errors.

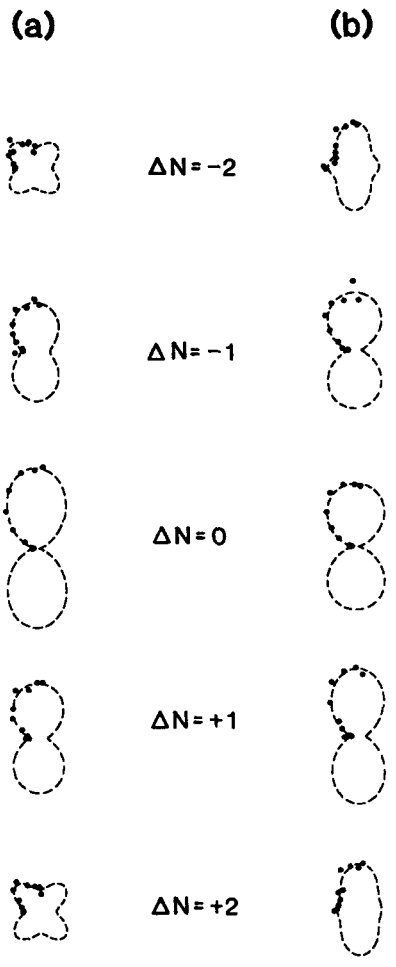

FIG. 7. Polar plots of the two-color photoelectron angular distributions for the five rotational peaks in Fig. 4. Excitation is via the $Q_{11} + P_{21}$ (25.5) transition. The angle χ between the laser polarization vectors is (a) 0° or (b) 90°. The dashed curves represent a fit of the data to Legendre polynomials as discussed in the text (see Table II); the solid circles are the measured data. In all cases, $\beta_0 \equiv 1.000$.

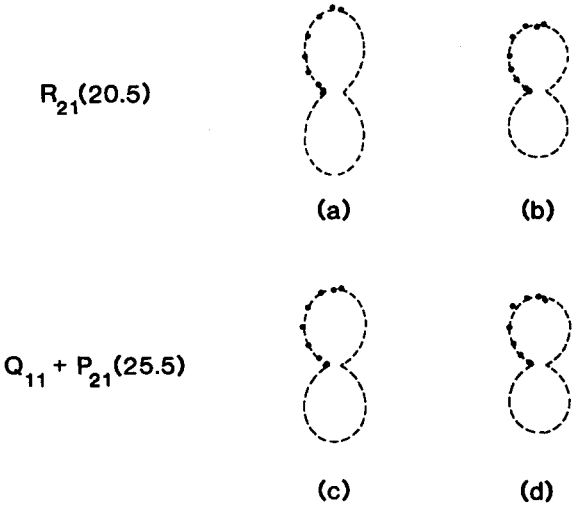

FIG. 6. Polar plots of the two-color photoelectron angular distributions for [(a),(b)] the NO A–X R_{21} (20.5) resonant excitation when the final rotational level of the ion is not resolved: (a) $\chi = 0°$ and (b) $\chi = 90°$; and [(c),(d)] the NO A–X $Q_{11} + P_{21}$ (25.5) resonant excitation when the final rotational level of the ion is not resolved: (c) $\chi = 0°$ and (d) $\chi = 90°$. The dashed curves represent fits to Eq. (2) in the text, where in (a) $\beta_0 \equiv 629.13$, $\beta_2 \equiv 1.534$, and $\beta_4 = 0.270$ ($r = 0.999$); in (b) $\beta_0 \equiv 764.89$, $\beta_2 \equiv 1.353$, and $\beta_4 = -0.105$ ($r = 0.998$); in (c) $\beta_0 \equiv 882.92$, $\beta_2 \equiv 1.589$, and $\beta_4 = 0.024$ ($r = 0.999$); and in (d) $\beta_0 \equiv 964.01$, $\beta_2 \equiv 1.436$, and $\beta_4 = -0.112$ ($r = 0.997$). All plots are presented by normalizing to $\beta_0 \equiv 1.000$.

IV. DISCUSSION

Nitric oxide is a diatomic molecule with 15 electrons. Its ground state has the electronic configuration $(1\sigma)^2\,(2\sigma)^2\,(3\sigma)^2\,(4\sigma)^2\,(5\sigma)^2\,(1\pi)^4\,(2\pi)^1, X\,^2\Pi$. The first excited state of NO involves the promotion of the electron in the unpaired 2π molecular orbital to the 6σ orbital, giving that state the symmetry designation $A\,^2\Sigma^+$. The NO $A\,^2\Sigma^+$ state is the first member of the $ns\sigma$ Rydberg series that converges to the $NO^+\,X\,^1\Sigma^+$ ion. As such, the 6σ orbital is often described as the $3s\sigma$ orbital, indicating that it is atomic-like in character. Electric-dipole-allowed photoionization of the NO $A\,^2\Sigma^+$ state is expected to produce a free electron in an outgoing p

TABLE II. $Q_{11} + P_{21}$ (25.5) excitation: angular distributions fit to Legendre polynomials.

		$\Delta N = -2$	$\Delta N = -1$	$\Delta N = 0$	$\Delta N = +1$	$\Delta N = +2$
(A) Raw data						
$\chi = 0°$	β_0	67.173	26.197	672.122	32.066	85.361
	β_2	0.246	0.890	1.922	1.203	0.382
	β_4	−0.442	−0.010	0.151	−0.097	−0.558
	r	0.850	0.981	0.999	0.991	0.935
$\chi = 90°$	β_0	66.378	41.649	730.800	46.764	78.423
	β_2	0.336	1.376	1.637	1.485	0.492
	β_4	0.349	−0.170	−0.204	0.115	0.251
	r	0.929	0.973	0.997	0.991	0.955
(B) Calculated values based on fit to model with $Q_{11} + P_{21}$ (25.5) excitation data						
$\chi = 0°$	β_0	55.289	27.523	663.784	29.942	55.764
	β_2	0.105	1.246	1.877	1.255	0.171
	β_4	−0.361	−0.151	0.017	−0.128	−0.278
$\chi = 90°$	β_0	75.225	44.292	654.837	45.405	60.247
	β_2	0.278	1.322	1.892	1.320	0.158
	β_4	0.145	0.047	−0.009	0.042	0.129
(C) Prediction based on fit to model with R_{21} (20.5) excitation data						
$\chi = 0°$	β_0	69.071	46.551	516.237	49.406	64.611
	β_2	0.052	0.710	1.780	0.723	0.192
	β_4	−0.114	−0.346	0.002	−0.299	0.024
$\chi = 90°$	β_0	119.471	44.261	493.534	45.532	76.243
	β_2	0.373	0.786	1.822	0.780	0.200
	β_4	0.052	0.182	−0.001	0.162	−0.010

wave. From angular momentum and parity conservation it can be shown[25,42] that photoionization of a Σ state to yield an ion in a Σ state obeys the selection rule

$$(N^+ - N_1) + l = \text{odd}, \tag{3}$$

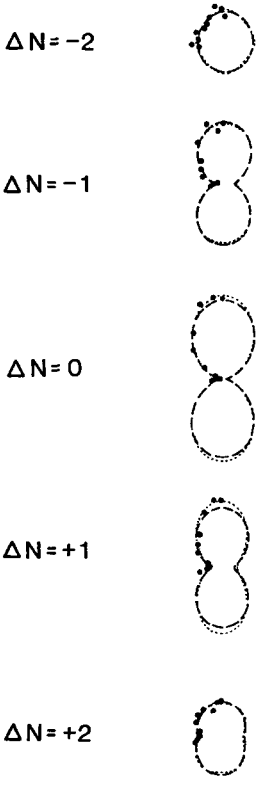

FIG. 8. Polar plots of the two-color photoelectron angular distributions for the five rotational peaks in Fig. 3. Excitation is via the R_{21} (20.5) transition. The angle χ between the electric field vectors of the two lasers is 54.7°. The solid circles are the measured data. The two curves represent fits of the data to Legendre polynomials as discussed in the text; the dashed curves represent a fit including only $P_0(\cos\theta)$ and $P_2(\cos\theta)$, while the dotted curves represent a fit including $P_0(\cos\theta)$, $P_2(\cos\theta)$, and $P_4(\cos\theta)$. In all cases, we have set $\beta_0 \equiv 1.000$ for plotting.

where $N^+ - N_1 = \Delta N$ is the change in the (molecular framework) rotational angular momentum in the photoionization process, and l is the orbital angular momentum quantum number of the departing photoelectron. To a first approximation, the application of Eq. (3) to the photoionization of the NO $A\,^2\Sigma^+$ state suggests the following behavior. The photoelectron energy spectrum should consist of three peaks corresponding to $\Delta N = 0$ and $\Delta N = \pm 2$, because $l = 1$ for an outgoing p wave. Additionally, the angular distribution might reflect simply the $\cos^2\theta$ behavior characteristic of s orbital photoionization.

Our observations contradict this picture. First, the presence of $\Delta N = \pm 1$ photoelectron peaks indicates contributions from even partial waves to the photoionization process. Second, the shape of the $\Delta N = \pm 2$ angular distribution [note the presence of two nodes in the $Q_{11} + P_{21}$ (25.5) distributions shown in Fig. 7] cannot arise from a pure p-wave transition; there must also be contributions from f waves or higher odd waves.

The departure from the united atom picture for the photoionization of the NO $A\,^2\Sigma^+$ state has two sources. First, an *ab initio* single-center expansion of the resonant intermediate 6σ orbital about the center of mass shows 94.0% s character, 0.3% p character, 5.4% d character, 0.1% f character, and 0.2% g character.[28] The small percentages of odd-l character of the state are not sufficient, however, to account for the observed $\Delta N = \pm 1$ transitions [see Table I(A)]. An additional factor is the nonspherical nature of the electron–molecular ion potential. This causes l mixing in the ionization continuum so that the l which contributes to the photoelectron angular distribution is not simply given by $l = l_0 \pm 1$, where l_0 is the l character of the single-center

expansion. We expect great sensitivity to the nonspherical nature of the ion potential because the energy of the ejected photoelectrons is quite low. It is the convolution of these two effects, the mixed l character of the intermediate state and the l mixing in the ionization continuum, which gives rise to the observed photoelectron energy and angular distributions.

One method for describing the photoionization of the NO $A\,^2\Sigma^+$ state is to carry out *ab initio* calculations directly incorporating these two effects. This is explored in detail in the following paper by Rudolph and McKoy.[29] We pursue here a different approach which relies only on the experimentally determined observables, the angular distributions for each ΔN photoelectron peak. We attempt to extract from these observables the contributions of different partial waves expressed in the molecular frame, both their relative magnitudes and phase relations. We also estimate the orientation of the transition dipole moment in the molecular frame by determining the fraction of parallel character in the photoionization transition. In the classical limit, the transition dipole moment is along the internuclear axis for a parallel transition and is at right angles to this axis for a perpendicular transition.

We describe the REMPI process as two separate events.[10] The first step is resonant excitation using plane-polarized light from an isotropic ground state to create an aligned intermediate state, i.e. $|J_g M_{Jg}\rangle \rightarrow |J_1 M_J\rangle$. The second step is photoionization of this excited state, i.e., $|J_1 M_J\rangle \rightarrow |J^+ M_J^+\rangle$. Prior to the second step, the excitation process has provided us with a distribution of M_J substates. In the absence of M_J-mixing interactions, each of these substates will be ionized independently. Thus, we can regard the photoionization process as a sum of separate M_J channels. A given $|J_1 M_J\rangle$ substate will have a series of transition probabilities which connect it with various final states. In other words, each M_J can populate several J^+'s, and several M_J^+'s within each J^+. Additionally, each $|J_1 M_J\rangle \rightarrow |J^+ M_J^+\rangle$ transition will produce a distribution of l,m,λ electrons. Here, m is the projection of the photoelectron orbital angular momentum l on the space-fixed quantization axis (which is taken as the electric vector of the ionization field), and λ is the projection on the molecular axis. Hence, each M_J can be considered to have its own angular distribution, which could be measured if we prepared a single $|J_1 M_J\rangle$ state.

The observed energy and angular distributions, then, are a sum of the individual M_J's energy and angular distributions, each weighted by the relative population in the M_J substate after resonant excitation. We express this as

$$I_\chi(J^+,\theta) = \sum_{M_J}\sum_{J_1} \mathrm{Prob}_\chi(J_g,M_{Jg} \Rightarrow J_1,M_J) \times \mathrm{Prob}(J_1,M_J \Rightarrow J^+,\theta), \tag{4}$$

where I_χ is the intensity measured for a given (J^+,θ) when θ is the angle between the electric field vector of the ionization laser and the detection axis, and χ is the angle between the polarization vectors of the excitation and ionization lasers. The summation over J_1 includes the possibility that several J_1's in the intermediate state are populated in the excitation step (e.g., through a blended transition). The development of this equation is discussed in Appendix A. The resulting model equation follows:

$$\begin{aligned} I_\chi(J^+,\theta) = \frac{4\pi}{3} N \Big\{ & a_{i1}F_s + a_{i2}F_p\Gamma_p + \frac{1}{2}a_{i3}F_p(1-\Gamma_p) + a_{i4}F_d\Gamma_d + \frac{1}{2}a_{i5}F_d(1-\Gamma_d) + a_{i6}F_f\Gamma_f + \frac{1}{2}a_{i7}F_f(1-\Gamma_f) \\ & + a_{i8}F_p[\Gamma_p(1-\Gamma_p)/2]^{1/2}\cos(\Delta_{p\sigma-p\pi}) + a_{i9}F_d[\Gamma_d(1-\Gamma_d)/2]^{1/2}\cos(\Delta_{d\sigma-d\pi}) \\ & + a_{i10}F_f[\Gamma_f(1-\Gamma_f)/2]^{1/2}\cos(\Delta_{f\sigma-f\pi}) \\ & + a_{i11}(F_sF_d\Gamma_d)^{1/2}\cos(\Delta_{s\sigma-d\sigma}) + a_{i12}[F_sF_d(1-\Gamma_d)/2]^{1/2}\cos(\Delta_{s\sigma-d\sigma}+\Delta_{d\sigma-d\pi}) \\ & + a_{i13}[F_p\Gamma_pF_f\Gamma_f]^{1/2}\cos(\Delta_{p\sigma-f\sigma}) + a_{i14}[F_p\Gamma_pF_f(1-\Gamma_f)/2]^{1/2}\cos(\Delta_{p\sigma-f\sigma}+\Delta_{f\sigma-f\pi}) \\ & + a_{i15}[F_p(1-\Gamma_p)F_f\Gamma_f/2]^{1/2}\cos(\Delta_{p\sigma-f\sigma}-\Delta_{p\sigma-p\pi}) \\ & + \frac{1}{2}a_{i16}[F_p(1-\Gamma_p)F_f(1-\Gamma_f)]^{1/2}\cos(\Delta_{f\sigma-f\pi}-\Delta_{p\sigma-p\pi}+\Delta_{p\sigma-f\sigma})\Big\}, \end{aligned} \tag{5}$$

where $F_f = (1 - F_s - F_p - F_d)$.

Not counting the normalization constant N, there are four types of terms in this equation. First, F_l refers to the fraction of l character contributing to the outgoing photoelectron wave. Second, Γ_l is the fraction of parallel character in the given l wave, i.e.,

$$\Gamma_l = \frac{r^2(l,\sigma)}{r^2(l,\sigma) + 2r^2(l,\pi)}, \tag{6}$$

where $r^2(l,\lambda)$ is the squared radial matrix element which connects the intermediate $|J_1 M_J\rangle$ state with an l-partial wave in the ionization continuum for a parallel ($\lambda = 0$; σ channel) or perpendicular ($\lambda = \pm 1$; π channel) photoionization transition. Third, $\Delta_{l\lambda-l'\lambda'}$ is the relative phase between the $l\lambda$ and $l'\lambda'$ partial waves expressed in the molecular frame. Last, a_{ij} is a coefficient which is evaluated by summing over a series of 3-j symbols as described in Appendix A. The coefficient a_{ij} depends on the angles θ and χ and

on the angular momentum quantum numbers involved in the specific photoionization transition.

Equation (5) predicts the photoelectron intensity observed when the ion is left in the rotational level J^+. This nonlinear equation contains 12 parameters. A given partial wave will contribute to either the even ΔN peaks or the odd ΔN peaks but not both. Nevertheless, we retain information about the relative importance of all of the partial wave contributions since our experiment allows us to measure the relative intensities of the different peaks. The different partial wave contributions are related in our model by N, the normalization constant. Thus, the different partial waves expressed in the molecular frame can be independently determined to within a phase factor in this model.

We fit Eq. (5) to 100 measured intensities (which are the combinations of 10 θ's, 2 χ's, and 5 J^+'s) from excitation via the $Q_{11}+P_{21}$ (25.5) transition. Table III presents the solution set of the "best" (smallest chi-squared residual) result of this calculation. Uncertainties in the parameters have been estimated based on the scatter in values from the top 10% iterations of the fitting process. We did not expect accurate determination of all the parameters given the scatter in the experimental data and the relative areas of the different photoelectron peaks. For example, the small (yet nonnegligible) fraction of d-wave character made fitting Γ_d difficult. Additionally, in the region around the best fit, Γ_f was found to be usually 0.0 but occasionally it was 1.0, indicating that this parameter was not determined by the fitting procedure. In what follows, Γ_f was fixed arbitrarily at 0.0. Table IV presents the squared moduli of the radial matrix elements relative to the $p\sigma$ channel (see Appendix A for the conversion relations).

As expected for photoionization of the $3s\sigma$ orbital of the NO $A\,^2\Sigma^+$, the $l=1$ partial wave dominates the ionization transition ($F_p=0.70$). The next most important contribution is the $l=3$ partial wave ($F_f=0.21$). The even partial waves add up to only 9% of the ionization continuum ($F_s=0.07$ and $F_d=0.02$). However, this is approximately an order of magnitude more than expected on the basis of the aforementioned single-center expansion.[28] The $p\sigma$–$p\pi$, and $d\sigma$–$d\pi$ pairs of partial waves are found to be 180° out of phase with each other (see Table III). This suggests that destructive interference is an important factor in the observed angular distributions.

TABLE III. Results from fit of Eq. (5).

	$Q_{11}+P_{21}$ (25.5)	R_{21} (20.5)
F_s	0.07 ± 0.01	0.00 ± 0.01
F_p	0.70 ± 0.05	0.61 ± 0.01
F_d	0.02 ± 0.01	0.15 ± 0.01
F_f[a]	0.21 ± 0.05	0.23 ± 0.02
Γ_p	0.42 ± 0.10	0.3 ± 0.25
Γ_d	0.2 ± 0.3	0.8 ± 0.3
Γ_f	0[b] ± 1	0.6 ± 0.15
$\Delta(p\sigma - p\pi)$	$173° \pm 10°$	$150° \pm 30°$
$\Delta(d\sigma - d\pi)$	$150° \pm 20°$	$70° \pm 60°$
$\Delta(f\sigma - f\pi)$	$35° \pm 10°$	$20° \pm 20°$
$\Delta(s\sigma - d\sigma)$	$15° \pm 10°$	$145° \pm 40°$
$\Delta(p\sigma - f\sigma)$	$90° \pm 90°$	$90° \pm 40°$

[a] This parameter is derived from the relation $F_f = 1.00 - F_s - F_p - F_d$.
[b] This parameter was undetermined by the fitting procedure and was fixed arbitrarily at this value.

TABLE IV. Squared moduli of the radial matrix elements.

	$Q_{11}+P_{21}$ (25.5)[a]		R_{21} (20.5)[b]	
	σ channel	π channel	σ channel	π channel
s	0.24		0.00	
p	1.00	0.69	0.86	1.00
d	0.01	0.02	0.56	0.07
f	0.0[c]	0.36	0.65	0.22

[a] Relative to the $p\sigma$ channel.
[b] Relative to the $p\pi$ channel.
[c] Γ_f was undetermined and fixed arbitrarily at 0.0.

The results of our calculation may be best appreciated graphically. We use the values in Table III to calculate the expected angular distributions for photoionization after a $Q_{11}+P_{21}$ (25.5) resonant excitation. These distributions are plotted in Fig. 9 as solid lines; filled circles represent the

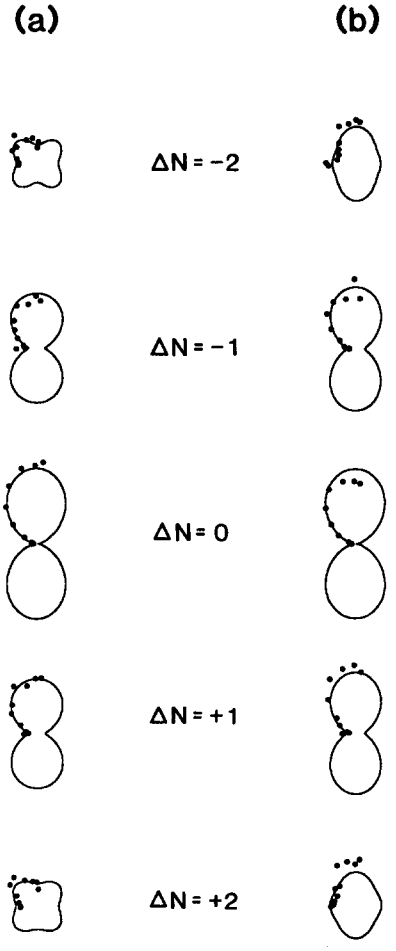

FIG. 9. Polar plots of the predicted two-color photoelectron angular distributions for excitation via the $Q_{11}+P_{21}$ (25.5) transition. The prediction is based on a fit of the $Q_{11}+P_{21}$ (25.5) excitation data to Eq. (5). The angle χ between the laser polarization vectors is (a) 0° or (b) 90°.

measured data points. We have fit the predicted angular distributions to Eq. (2) for normalization purposes; the results of this fit are presented in Table II(B). Again, the relative sizes of the different distributions arise by setting $\beta_0 \equiv 1.000$ for the plots. The $\Delta N = 0$ curves fit the measured points quite well. This is not surprising because most of the observed photoelectron intensity is produced by these transitions. The measured data for the $\Delta N \neq 0$ peaks have less intensity and thus a lower signal-to-background ratio. They provide a less consistent contribution to the fitting process because of their scatter. The angular distributions predicted by our fitting process for these peaks, however, are in good agreement with the distributions (dashed lines) presented in Fig. 7.

The above analysis was based on a fit to the alignment in the intermediate state produced by the $Q_{11} + P_{21}$ (25.5) transition. The information we have obtained about the photoionization process is independent of the resonant excitation process. Thus, we can use the values for the parameters presented in Table III to predict the angular distributions observed when different intermediate state alignments are prepared. Appendix B discusses the effect of the intermediate state alignment. Figure 10 presents the angular distributions predicted for excitation via the R_{21} (20.5) transition, based on the results from fitting the data from excitation via the $Q_{11} + P_{21}$ (25.5) transition. Parameters from fitting this prediction to Legendre polynomials [Eq. (2)] are listed in Table I(C). The predictions are seen to be consistent with the observed angular distributions, presented as filled circles.

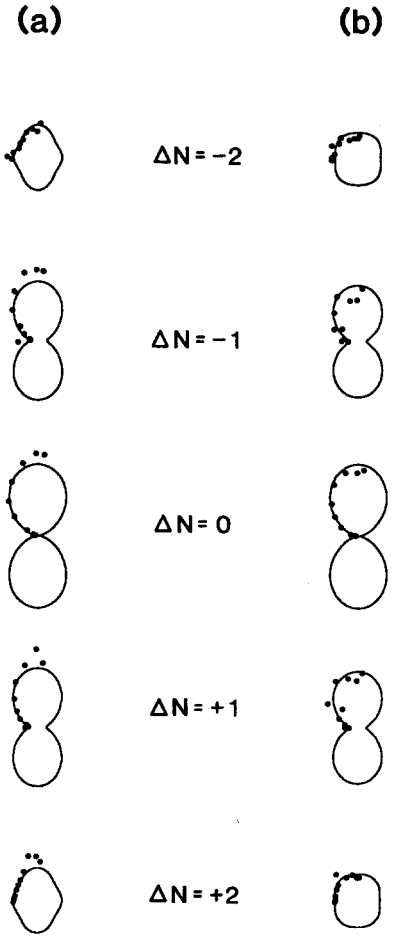

FIG. 10. Polar plots of the predicted two-color photoelectron angular distributions for excitation via the R_{21} (20.5) transition.The prediction is based on a fit of the $Q_{11} + P_{21}$ (25.5) excitation data to Eq. (5). The angle χ between the laser polarization vectors is (a) 0° or (b) 90°. In all cases, $\beta_0 \equiv 1.000$.

It is interesting to compare the predicted angular distributions in Figs. 9(b) and 10(a). They are similar, which suggests that an intermediate state with similar alignment is being photoionized. However, the $\Delta N = \pm 2$ distributions in Figs. 9(a) and 10(b) exhibit different extremes of behavior. The nodes in Fig. 9(a) are predicted to be more pronounced than in Fig. 10(b). Examination of the alignment prepared in these cases shows that the differences in the angular distributions of the $\Delta N = \pm 2$ peaks can be directly correlated to the differences in the intermediate state alignment, that is, the more isotropic angular distribution arises from photoionization of the less aligned intermediate state. This is discussed further in Appendix B. The different extremes in the predicted angular distributions are consistent with the measured angular distributions [see Figs. 5(b) and 7(a), and the angular distributions taken at the magic angle, shown in Fig. 8].

We have also used our model to perform a fit of the experimental data obtained using the R_{21} (20.5) excitation. The results, presented in Tables III and IV, are similar to the results obtained when fitting the $Q_{11} + P_{21}$ (25.5) excitation data. The agreement of these independent fits gives us confidence in the validity of our model and in the nonlinear fitting procedure employed.

We use the results from the fit to the R_{21} (20.5) excitation data to calculate the angular distributions following excitation via this R_{21} (20.5) transition (Fig. 11), and to predict the angular distributions following excitation via the $Q_{11} + P_{21}$ (25.5) transition (Fig. 12). The shape of each distribution is consistent with that measured (see Figs. 5 and 7); however, it is evident from Figs. 11 and 12 that the use of the R_{21} (20.5) excitation data provides parameters that are somewhat less successful in fitting the measured distributions. Nevertheless, we believe that the parameters listed in Table III represent a self-consistent description of the photoionization event.

An advantage of our model is the ability to decompose the predicted angular distributions into a sum of contributions from the different partial waves. This allows us to determine directly the source of the observed distribution. We performed such a partial wave decomposition using the results of our fitting procedure.[43] We find that the intensity in the $\Delta N = 0$ photoelectron peak comes mostly from $p\sigma$ and $p\pi$ partial waves, and constructive $p\sigma$–$p\pi$ interference. The f-partial wave contributes only 5% to 10% as much as the p-partial waves. Interference between $p\sigma$–$f\pi$ and $p\pi$–$f\pi$ partial wave channels has both constructive and destructive components; the net effect of these interfering channels is almost complete cancellation. These factors combine to produce an angular distribution well described as $\cos^2 \theta$.

The $\Delta N = \pm 1$ peaks have contributions from s and d waves. The $s\sigma$ waves contribute equally at all angles. The $d\pi$

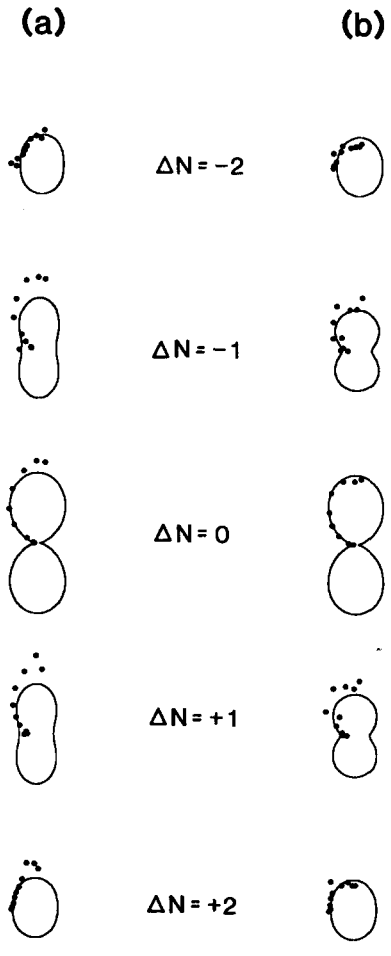

FIG. 11. Polar plots of the predicted two-color photoelectron angular distributions for excitation via the R_{21} (20.5) transition.The prediction is based on a fit of the R_{21} (20.5) excitation data to Eq. (5). The angle χ between the laser polarization vectors is (a) 0° or (b) 90°. In all cases, $\beta_0 \equiv 1.000$.

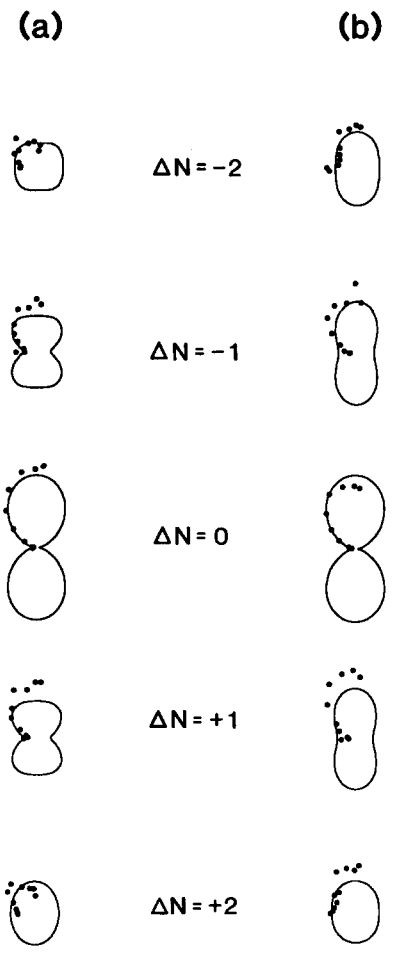

FIG. 12. Polar plots of the predicted two-color photoelectron angular distributions for excitation via the $Q_{11} + P_{21}$ (25.5) transition.The prediction is based on a fit of the R_{21} (20.5) excitation data to Eq. (5). The angle χ between the laser polarization vectors is (a) 0° or (b) 90°. In all cases, $\beta_0 \equiv 1.000$.

contribution is approximately four times more important than that of the $s\sigma$ partial waves; both contributions peak at 0° and diminish at 90°. However, even more important to the angular distribution are the $s\sigma$–$d\sigma$ and $s\sigma$–$d\pi$ interferences which are constructive at 0° (contributing as much as the $s\sigma$ partial wave) but strongly destructive at 90°.

The angular distribution of the $\Delta N = \pm 2$ peaks requires strong f-wave participation. Our decomposition indicates that the $p\sigma$ and $p\pi$ contributions are canceled by the destructive interference between these two channels. The $f\pi$ contribution is enhanced by the constructive interference between the p and f channels (there is no $f\sigma$ contribution because Γ_f was fixed at 0.0). The interferences between the p and f waves (e.g., $p\sigma$–$f\pi$) is both constructive and destructive, with very little net effect at all angles. Thus, the shapes of the $\Delta N = \pm 2$ angular distributions are primarily determined by the f-partial wave contribution.

Only an insignificant intensity was observed at the flight time appropriate for $\Delta N = \pm 3$ photoelectrons, and no signal was observed for $\Delta N = \pm 4$. These two observations confirm our approximation that partial waves of $l > 3$ do not contribute to the scattering dynamics. Thus, only d waves contribute to the $\Delta N = \pm 3$ peaks in our model. The predicted intensity in this peak is only 1% of that predicted for the $\Delta N = \pm 2$ photoelectron peaks because of destructive interference between the $d\sigma$ and $d\sigma$ partial waves. This small intensity would be lost in the background signal. Similarly, our model allows only f waves to contribute to $\Delta N = \pm 4$ photoionization transitions. Choosing $\Gamma_f \equiv 0.00$ restricts the $l = 3$ contributions to $f\pi$ partial waves. We predict the $\Delta N = \pm 4$ peaks to have 25% of the intensity of the $\Delta N = \pm 2$ peaks, which may be observable. Choosing a slightly different set of parameter, with $\Gamma_f = 0.5$, provides shapes consistent with those observed for all ΔN peaks. In this case, interference between $f\pi$ and $f\sigma$ partial waves is predicted to remove almost all of the intensity of the $\Delta N = \pm 4$ peaks. We therefore believe the value chosen for Γ_f explains the overgenerous prediction for signal in the $\Delta N = \pm 4$ peaks.

There have been two recent studies of the fraction of parallel character in photoionization of the NO $A\,^2\Sigma^+$ state. First, Jacobs, Madix, and Zare[33] investigated the role of saturation in the resonant excitation step of REMPI in determining rovibrational population distributions. Their study included a detailed consideration of the effects of laser power as well as the effects of an initially aligned ground state on

the observed REMPI signal. They examined $(1+1)$ REMPI of NO via its $A\,^2\Sigma^+$ state. Because they detected photoions rather than photoelectrons, they were forced to average over more final state information, such as the final rotational state of the ion and the partial wave composition of the photoelectron. They found $\Gamma_{\text{total}} = 0.461^{+0.06}_{-0.10}$. Second, *ab initio* calculations by Rudolph and McKoy[29] indicate $\Gamma_{\text{total}} = 0.280$.

Using our results, we find the fraction of parallel character in the photoionization transition to be $\Gamma_{\text{total}} = 0.37 \pm 0.22$ for the $Q_{11} + P_{21}$ (25.5) excitation data, and $\Gamma_{\text{total}} = 0.44 \pm 0.16$ for the R_{21} (20.5) excitation data. Unfortunately, we are unable to choose definitively between the previous experimental result or the *ab initio* calculation, as our values for Γ_{total} are consistent with both, given our uncertainty. Two-thirds of the uncertainty in our calculation is caused by the uncertainty in the undetermined parameter Γ_f. Our estimate of Γ_{total} is surely too low as any choice of $\Gamma_f > 0.0$ will increase Γ_{total} significantly because $F_f = 0.22$. Thus, the present experiment does favor the value for Γ_{total} given by Jacobs *et al.*,[33] and is consistent with the conclusion of Jacobs *et al.* that the total photoionization cross section is relatively insensitive to the intermediate state alignment.

In conclusion, the ability to perform angle- and energy-resolved photoelectron spectroscopy allows the determination of detailed information about the photoionization process, namely, the fraction of parallel character in the photoionization transition and the relative contributions and relative phase shifts of the participating photoelectron partial waves expressed in the molecular frame. This facilitates quantitative comparison with *ab initio* calculations.[25–28] Although we have demonstrated this technique for a diatomic system, the extension to polyatomic molecules is straightforward. From the experimental data alone, the photoionization continuum may be decomposed into a small number of interfering partial waves for the outgoing photoelectron expressed in the symmetry of the molecular frame.

ACKNOWLEDGMENTS

We would like to thank H. Rudolph and V. McKoy for many helpful discussions and communication of results prior to publication. Support of the Air Force Office of Scientific Research under AFOSR F49620-86-C-0016 is gratefully acknowledged.

APPENDIX A

In this Appendix we present the framework for the development of our model. We employ the standard nomenclature defined in Table V. Both the intermediate and the ion states of NO are treated using the appropriate angular momentum quantum numbers for Hund's case (b).[39]

The starting point for this derivation was given in Eq. (4).

$$I_\chi(J^+,\theta) = \sum_{M_J}\sum_{J_1} \text{Prob}_\chi(J_g,M_{Jg} \Rightarrow J_1,M_J) \times \text{Prob}(J_1,M_J \Rightarrow J^+,\theta). \quad \text{(A1)}$$

TABLE V. Nomenclature.

$\mathbf{N}_1$	=	Angular momentum due to nuclear rotation and orbital angular momentum of the excited state, with space-fixed and molecule-fixed projections M_1 and Λ_1.
$\mathbf{N}^+$	=	Angular momentum due to nuclear rotation and orbital angular momentum of the ground state of the ion, with space-fixed and molecule-fixed projections M^+ and Λ^+.
$\mathbf{N}_t$	=	Angular momentum transferred to the molecular ion, with space-fixed and molecule-fixed projections m_t and λ_t.
$\mathbf{J}_g$	=	Total angular momentum of the ground state apart from nuclear spin, with space-fixed and molecule-fixed projections M_g and Ω_g [Hund's case (a)].
$\mathbf{J}_1$	=	Total angular momentum of the excited state apart from nuclear spin, with space-fixed projection M_J [Hund's case (b)].
$\mathbf{J}^+$	=	Total angular momentum of the ground state of the ion apart from nuclear spin, with space-fixed projection M_J^+.
$\mathbf{S}_1$	=	Total electron spin of excited state, with space-fixed projection M_S^1.
$\mathbf{S}^+$	=	Total electron spin of the ion core, with space-fixed projection M_S^+.
$\mathbf{l}$	=	Orbital angular momentum of the photoelectron in partial wave l, with space-fixed and molecule-fixed projections m and λ.
μ_0	=	Space-fixed projection of the dipole photon's unit angular momentum.
μ	=	Molecule-fixed projection of the dipole photon's unit angular momentum.
θ	=	Angle of the ionization laser polarization with respect to the detection axis of the TOF apparatus.
χ	=	Angle between the polarization vectors of the resonant and ionization lasers.

The probability of populating a given $|J_1,M_J\rangle$ substate of the intermediate state can be expressed as

$$\text{Prob}_\chi(J_g,M_{Jg} \Rightarrow J_1,M_J) \propto \sum_{M_{Jg}} S(J_g,J_1)\left[d^{J_1}_{M_{Jg},M_J}(\chi)\right]^2 \times \begin{pmatrix} J_g & 1 & J_1 \\ -M_{Jg} & 0 & M_{Jg} \end{pmatrix}^2. \quad \text{(A2)}$$

In this expression the 3-j symbol shows the alignment of the intermediate state created by using a plane-polarized excitation field. The reduced rotational matrix element $d^{J_1}_{M_{Jg},M_J}(\chi)$ transforms the alignment created in the frame of the excitation laser into that observed in the frame of the ionization laser. The transition we consider is the $Q_{11} + P_{21}$ (25.5) resonant transition that is blended and produces a mixture of $J_1 = 24.5$ and $J_1 = 25.5$ ($N_1 = 25$ in both cases) in the intermediate state; thus, the population in each J_1 is weighted by the appropriate rotational line strengths $S(J_g,J_1)$.[38] We assume that the intermediate levels are incoherently excited because of the temporal and spatial inhomogeneity of the excitation radiation.[28] Consequently, we perform the sum over J_1 in an incoherent manner. Photoionization occurs during the 6 ns laser pulse before M_J-mixing events, such as hyperfine depolarization or collisions, can occur. Thus, we perform the sum over M_J incoherently as well.

To discuss the photoionization portion of Eq. (A1), we take as a starting place Eq. (6) of Dixit *et al.*[25] A similar equation has been derived by a number of authors.[10,34,44] We prefer this form as it properly includes the effects of spin on the photoionization process:

$$\langle \text{final}|D_{\mu_0}|\text{int}\rangle = \langle \gamma_f \Lambda^+ N^+ S^+ J^+ M_J^+; m_\sigma | D_{\mu_0} | \gamma_i \Lambda_1 N_1 S_1 J_1 M_J \rangle$$

$$= \left(\frac{4\pi}{3}\right)^{1/2} [(2N_1+1)(2N^++1)(2J_1+1)(2J^++1)(2S_1+1)]^{1/2}$$

$$\times \sum_{l,m,N_t,m_t,M_1,M_S^1,M^+,M_S^+} Y_{lm}(\theta,\phi)(2N_t+1)(-1)^P \begin{pmatrix} N_1 & S_1 & J_1 \\ M_1 & M_S^1 & -M_J \end{pmatrix}$$

$$\times \begin{pmatrix} N^+ & S^+ & J^+ \\ M^+ & M_S^+ & -M_J^+ \end{pmatrix} \begin{pmatrix} S^+ & 1/2 & S_1 \\ M_S^+ & m_\sigma & -M_S^1 \end{pmatrix} \begin{pmatrix} N^+ & N_1 & N_t \\ -M^+ & M_1 & m_t \end{pmatrix} \begin{pmatrix} N_t & 1 & l \\ m_t & \mu_0 & -m \end{pmatrix}$$

$$\times (-i)^l \exp(i\eta_{l\lambda\mu}) \left\{ \sum_{\mu,\lambda,\lambda_t} \bar{r}(i,f;\mu,l) \begin{pmatrix} N^+ & N_1 & N_t \\ -\Lambda^+ & \Lambda_1 & \lambda_t \end{pmatrix} \begin{pmatrix} N_t & 1 & l \\ -\lambda_t & \mu & -\lambda \end{pmatrix} \right\}. \tag{A3}$$

In this equation, D_{μ_0} is the transition electric dipole moment operator,

$$\bar{r}(i,f;\mu,l) = \int \chi_{\text{vib}}^{(f)} \left\langle \Psi_{\text{elec}}^{(f)} \left| \sum_s r_s Y_{1\mu}(r_s) \right| \Psi_{\text{elec}}^{i} \right\rangle \chi_{\text{vib}}^{i} \, dR \tag{A4}$$

is the radial integral of this operator,

$$P = M^+ - \Lambda^+ + \mu_0 - N_1 + S_1 - M_J + N^+ + M_J^+ - \tfrac{1}{2} + M_S^1, \tag{A5}$$

and γ_i, γ_f contain all other quantum numbers needed for the unambiguous designation of the intermediate and final states, respectively. We adapt this to REMPI via the NO $A\,^2\Sigma^+$ state. For this case, $\Lambda_1 = \Lambda^+ = 0$, which causes $\lambda_t = 0$ as well as $\lambda = \mu$. The use of linearly polarized light sets $\mu_0 = 0$, so that $m_t = -m$. We group the radial integral and phase shift $\eta_{l\lambda\mu}$ of the departing photoelectron using

$$R(l\lambda\eta) = (-i)^l \exp(i\eta_{l\lambda\lambda})\, \bar{r}(i,f;\mu,l). \tag{A6}$$

These radial matrix elements are calculable by *ab initio* methods, such as those used by McKoy and co-workers.[25–29] It is their magnitudes and phases that control the dynamics of the photoionization process and determine the shape of the angular distribution. We have included the phase factor $\eta_{l\lambda\lambda}$ to remind us that each partial wave will have both a magnitude and a phase; it is the relative phases of the outgoing waves which can give rise to interferences between these partial waves.

Simplication of Eq. (A3) yields

$$\langle \text{final}|D_{\mu_0}|\text{int}\rangle = \langle \gamma_f J^+ M_J^+; m_\sigma | D_{\mu_0} | \gamma_i \Lambda_1 N_1 S_1 J_1 M_J \rangle$$

$$= \left(\frac{4\pi}{3}\right)^{1/2} [(2N_1+1)(2J^++1)(2J_1+1)]^{1/2} (-1)^{-N_1 - M_J - M_J^+ + 1/2}$$

$$\times \sum_{l,m,N_t,M_S^1} Y_{lm}(\theta,\phi)(2N_t+1) \begin{pmatrix} N_1 & 1/2 & J_1 \\ M_1 & M_S^1 & -M_J \end{pmatrix} \begin{pmatrix} J^+ & N_1 & N_t \\ -M_J^+ & M_1 & -m \end{pmatrix}$$

$$\times \begin{pmatrix} N_t & 1 & l \\ m & 0 & -m \end{pmatrix} \begin{pmatrix} J^+ & N_1 & N_t \\ 0 & 0 & 0 \end{pmatrix} \left\{ \sum_\lambda R(l\lambda\eta) \begin{pmatrix} N_t & 1 & l \\ 0 & \lambda & -\lambda \end{pmatrix} \right\}. \tag{A7}$$

This expression involves sums over l,m,N_t,M_S, and λ. Ultimately, we will square $\langle \gamma_f J^+ M_J^+; m_\sigma | D_{\mu_0} | \gamma_i \Lambda_1 N_1 S_1 J_1 M_J \rangle$ to obtain the transition probability. Because we measure the angle- and energy-resolved spectrum, we must allow for interferences between outgoing photoelectron channels. Thus, we sum over l and λ coherently, while the sums over N_t and m are performed incoherently.[3,45,46] Recognizing this, we can collect everything outside of the coherent sums into the following coefficient:

$$C(l,m,\lambda,N_t,N_1,J_1,M_J,J^+,M_J^+) = \sum_{M_S^1} Y_{lm}(\theta,\phi)(2N_t+1) \begin{pmatrix} N_1 & 1/2 & J_1 \\ M_J - M_S^1 & M_S^1 & -M_J \end{pmatrix} \begin{pmatrix} J^+ & N_1 & N_t \\ -M_J^+ & M_J - M_S^1 & -m \end{pmatrix}$$

$$\times \begin{pmatrix} N_t & 1 & l \\ m & 0 & -m \end{pmatrix} \begin{pmatrix} J^+ & N_1 & N_t \\ 0 & 0 & 0 \end{pmatrix} \begin{pmatrix} N_t & 1 & l \\ 0 & \lambda & -\lambda \end{pmatrix}$$

$$\equiv C(l\lambda). \tag{A8}$$

We explicitly write out the sum over l and λ in Eq. (A7). By applying 3-j symmetry relations,[25,39] we equate the $\lambda = \pm 1$ channels:

$$\langle \text{final}|D_{\mu_0}|\text{int}\rangle = \left(\frac{4\pi}{3}\right)^{1/2}[(2N_1+1)(2J_1+1)(2J^++1)]^{1/2}(-1)^{-N_1-M_J-M_J^++1/2}$$
$$\times \sum_{N_p m}[C(s\sigma)R(s\sigma,\eta)+C(p\sigma)R(p\sigma,\eta)+2C(p\pi)R(p\pi,\eta)$$
$$+C(d\sigma)R(d\sigma,\eta)+2C(d\pi)R(d\pi,\eta)+C(f\sigma)R(f\sigma,\eta)+2C(f\pi)R(f\pi,\eta)]. \quad \text{(A9)}$$

Here we have included up to f waves in the partial wave expansion.

Squaring this expression is straightforward and results in an expression with 28 terms. Seven of these terms are of the form

$$[C(l\lambda)]^2[R(l\lambda,\eta)]^2 \equiv [C(l\lambda)]^2 r^2(l\lambda), \quad \text{(A10a)}$$

while the remaining 21 products are off-diagonal terms of the form

$$C(l\lambda)C(l'\lambda')r(l\lambda)r(l'\lambda')\cos(\eta-\eta'). \quad \text{(A10b)}$$

Application of the $\Delta N + l =$ odd selection rule [Eq. (3)] implies that for production of a specific $J^+ (= N^+)$ from a single N_1, only even or odd partial waves will appear, not both. Consequently, cross products containing an even–odd pair of l contributions will vanish [i.e., $s\sigma$ waves will not populate the same values of J^+ as $p\sigma$ waves because terms containing $C(s\sigma)C(p\sigma)$ vanish for a given J^+]. This simplifies our expression to 16 terms, only 12 of which are independent. Seven of these terms will give us directly the value of $r^2(l\lambda)$; this can be used with the remaining five terms to deduce the relative phase shifts of the outgoing partial waves.

Combining the photoionization step with the excitation step we rewrite Eq. (A1) as

$$I_\chi(J^+,\theta) = \sum_{J_1,M_J,M_J^+} |\langle \gamma_f J^+ M_J^+; m_\sigma | D_{\mu_0} | \gamma_i \Lambda_1 N_1 S_1 J_1 M_J\rangle|^2 \sum_{M_{Jg}} S(J_g,J_1)[d^{J_1}_{M_{Jg},M_J}(\chi)]^2 \begin{pmatrix} J_g & 1 & J_1 \\ -M_{Jg} & 0 & M_{Jg}\end{pmatrix}^2. \quad \text{(A11)}$$

We define a new coefficient using our previous definition of $C(l\lambda)$:

$$a_{ij} \equiv \frac{4\pi}{3}(2N_1+1)(2J_1+1)(2J^++1)F(l\lambda,l'\lambda')$$
$$\times \sum_{M_{Jg},J_1,M_J,M_J^+,N_t,m} S(J_g,J_1)C(l,m,\lambda,N_t,N_1,J_1,M_J,J^+,M_J^+)$$
$$\times C(l',m,\lambda',N_t,N_1,J_1,M_J,J^+,M_J^+)[d^{J_1}_{M_{Jg},M_J}(\chi)]^2 \begin{pmatrix} J_g & 1 & J_1 \\ -M_{Jg} & 0 & M_{Jg}\end{pmatrix}^2. \quad \text{(A12)}$$

In Eq. (A12) the subscript j ranges between 1 and 16, and corresponds to the 16 different combinations of l, λ, l', and λ' which occur; the subscript i ranges between 1 and 100, and corresponds to the possible combination of J^+, θ, and χ. The factor $F(l\lambda,l'\lambda')$ is either 1, 2, 4, or 8; this arises from squaring Eq. (A9).

Using this definition of a_{ij} we can describe the intensity of the photoelectron signal corresponding to the production of NO ions in the rotational level J^+, measured with the plane of polarization of the ionization laser at an angle θ with respect to the detection axis, and with an angle χ between the planes of polarization of the excitation and ionization lasers as

$$I_\chi(J^+,\theta) = a_{i1}r^2(s\sigma)+a_{i2}r^2(p\sigma)+a_{i3}r^2(p\pi)+a_{i4}r^2(d\sigma)+a_{i5}r^2(d\pi)$$
$$+a_{i6}r^2(f\sigma)+a_{i7}r^2(f\pi)+a_{i8}r(p\sigma)r(p\pi)\cos(\Delta_{p\sigma-p\pi})$$
$$+a_{i9}r(d\sigma)r(d\pi)\cos(\Delta_{d\sigma-d\pi})+a_{i10}r(f\sigma)r(f\pi)\cos(\Delta_{f\sigma-f\pi})$$
$$+a_{i11}r(s\sigma)r(d\sigma)\cos(\Delta_{s\sigma-d\sigma})+a_{i12}r(s\sigma)r(d\pi)\cos(\Delta_{s\sigma-d\pi})$$
$$+a_{i13}r(p\sigma)r(f\sigma)\cos(\Delta_{p\sigma-f\sigma})+a_{i14}r(p\sigma)r(f\pi)\cos(\Delta_{p\sigma-f\pi})$$
$$+a_{i15}r(p\pi)r(f\sigma)\cos(\Delta_{p\pi-f\sigma})+a_{i16}r(p\pi)r(f\pi)\cos(\Delta_{p\pi-f\pi}). \quad \text{(A13)}$$

Each term in Eq. (A13) is composed of a constant a_{ij} and a variable $[r(l\lambda)r(l'\lambda')\cos(\eta-\eta')]$.

We reorganize the 16 variables and choose a normalization scheme so that the resulting 12 independent variables have physical meaning as described in Sec. IV. We define a normalization constant N such that

$$N = \sum_l [r^2(l\sigma)+2r^2(l\pi)]. \quad \text{(A14)}$$

Then the fraction of a given partial wave l is given by

$$F_l = \frac{r^2(l\sigma)+2r^2(l\pi)}{N}. \quad \text{(A15)}$$

Note that $F_f = 1 - F_s - F_p - F_d$. We also define the degree of parallel character for a given partial wave component as

$$\Gamma_l \equiv \frac{r^2(l\sigma)}{r^2(l\sigma) + 2r^2(l\pi)}, \tag{A16}$$

so that

$$\Gamma_{\text{total}} \equiv \sum_l F_l \Gamma_l. \tag{A17}$$

Here Γ_{total} represents the more familiar overall degree of parallel character of the photoionization transition. Substitution of these parameters into Eq. (A13) yields Eq. (5).

The calculation is performed as follows. First, the coefficients a_{ij} are calculated for the conditions of the experimental data. Second, the data are fit to Eq. (5) using these coefficients. The system of equations to be solved is a nonlinear system of 100 equations in 12 variables. We use the Newton–Raphson method[47] to find the roots of the following equation:

$$f_i(x_1,x_2,\ldots,x_{12}) - I_{\chi,\text{meas}}(J^+,\theta) = 0, \tag{A18}$$

where

$$f_i(x_1,x_2,\ldots,x_{12}) = I_\chi(J^+,\theta). \tag{A19}$$

Given initial "good" guesses at the roots of Eq. (A18), this method expands $f_i(\{x_k\})$ in the neighborhood of each x_k in a Taylor series, then neglects terms of order δx_k^2 and higher. In addition to initial values, this method requires evaluation of both $f_i(\{x_k\})$ and all the derivatives of $f_i(\{x_k\})$ at arbitrary x_k. Initial values are randomly generated for each trial. Because we have more data points than variables, we solve for the corrections to $f_i(\{x_k\})$ using a singular value decomposition method.[47] The corrections δx_k are added to the variables, the function is evaluated at the new values of the variables, and checked for convergence. If not converged, corrections to the variables are computed again. This iteration continues until either the variables stop changing or the function converges. In all cases convergence is observed only when the variables stop changing: the function is not observed to converge. At the best convergence of the variables the sum of the squares of the residuals for the 100 equations was on the order of 200 000, which corresponds to a deviation of about 45 for each data point (values of the data ranged from ~ 6 to ~ 2800). The results of this fit have been presented in Table III.

APPENDIX B

In this Appendix we discuss the alignment of the intermediate state. Recall that

$$\text{Prob}_\chi(J_g,M_{Jg} \Rightarrow J_1,M_J) \propto \sum_{M_{Jg}} S(J_g,J_1)\left[d^{J_1}_{M_{Jg},M_J}(\chi)\right]^2 \times \begin{pmatrix} J_g & 1 & J_1 \\ -M_{Jg} & 0 & M_{Jg} \end{pmatrix}^2. \tag{B1}$$

In this equation M_{Jg} is the projection of the ground state's rotational angular momentum $\mathbf{J}_g$ on the first step's quantization axis (the electric field vector of the excitation laser), and M_J is the projection of the intermediate state's rotational angular momentum $\mathbf{J}_1$ on the second step's quantization axis (the electric field vector of the ionization laser). Figure 13 is a histogram of the relative M_J populations after a $P(25.5)$ excitation transition for six different angles χ between the electric field vectors of the excitation and ionization lasers. Because of 3-j symmetry relations, an R branch excitation gives similar results. The extremes in alignment are observed when the two lasers are polarized parallel and orthogonal to each other, although the degree of alignment in Fig. 13(a) is much more severe than in Fig. 13(f). The transition from alignment along $\mathbf{J}_1$ (0°) to alignment normal to $\mathbf{J}_1$ (90°) is smooth as χ increases; at $\chi = 54.7°$ (the "magic angle"), the intermediate state is isotropic (all values of M_J are equally populated).

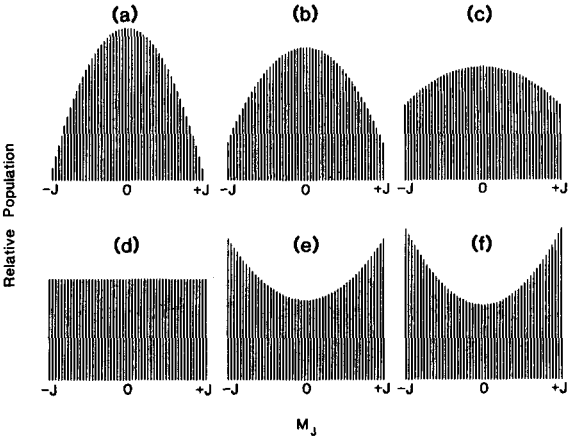

FIG. 13. The relative M_J populations in the intermediate state after excitation via a P (25.5) branch excitation. The angle χ between the laser polarization vectors is (a) $\chi = 0°$, (b) $\chi = 30°$, (c) $\chi = 45°$, (d) $\chi = 54.7°$, (e) $\chi = 70°$, or (f) $\chi = 90°$.

Figure 14 plots the relative M_J populations after a Q (25.5) excitation transition. As expected classically, the alignment is opposite to that from the P branch excitation. A comparison of Figs. 14(f) and 13(a) shows that the inversion of alignment is complete: the M_J populations in both

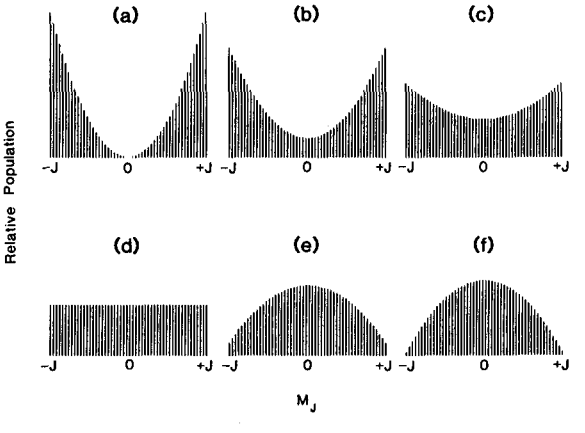

FIG. 14. The relative M_J populations in the intermediate state after excitation via a pure Q (25.5) branch excitation. The angle χ between the laser polarization vectors is (a) $\chi = 0°$, (b) $\chi = 30°$, (c) $\chi = 45°$, (d) $\chi = 54.7°$, (e) $\chi = 70°$, or (f) $\chi = 90°$.

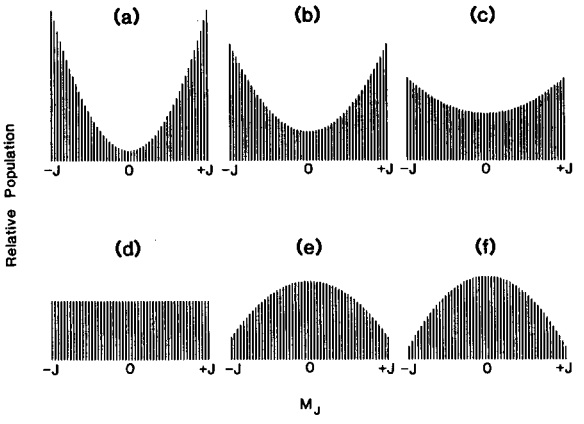

FIG. 15. The relative M_J populations in the intermediate state after excitation via a blended $Q+P$ (25.5) branch excitation. The ratio of rotational line strengths is 8:1, Q:P. The angle χ between the laser polarization vectors is (a) $\chi = 0°$, (b) $\chi = 30°$, (c) $\chi = 45°$, (d) $\chi = 54.7°$, (e) $\chi = 70°$, or (f) $\chi = 90°$.

cases are strongly peaked along $\mathbf{J}_1$ and decrease to zero normal to $\mathbf{J}_1$. This contrasts with the alignment demonstrated in Figs. 14(a) and 13(f). Although the trends are the same in these two figures, Fig. 13(f) predicts a more isotropic M_J distribution than Fig. 14(a). Because we are unable to completely resolve any "pure" Q branch transitions, we repeat our calculation for the mixed $Q_{11}+P_{21}$ (25.5) excitation. This transition is approximately 8:1 Q in character, so we expect to see mostly "Q" behavior in the intermediate state alignment. This is demonstrated in Fig. 15, which presents the intermediate state alignments predicted for a $Q_{11}+P_{21}$ (25.5) excitation. Evidently the small amount of P character does not dilute the alignment so severely as the pure R branch excitation.

Comparison of these M_J population plots with the $\Delta N = \pm 2$ angular distributions, both observed and predicted (Figs. 5, 7, 9, 10, 11, and 12), indicates a correlation between the degree of alignment and the anisotropy in the angular distribution. The alignment produced by R branch excitation is predicted to be more isotropic; the measured R_{21} (20.5) $\Delta N = \pm 2$ angular distributions (see Figs. 5, 10, and 11) are observed to be more isotropic than those from the blended $Q+P$ excitation (Figs. 7, 9, and 12). The presence of two nodes in the $\Delta N = \pm 2$ distributions indicate contributions from f waves; however, the lack of two nodes would not rule out f waves! Apparently, pronounced intermediate state alignment serves to expose the f-wave contributions. In all three cases (pure P, pure Q, and blended 8:1 $Q+P$) the M_J distribution is predicted to be isotropic when the angle between the two lasers is 54.7° (the magic angle). Under these conditions, the asymmetry in the measured angular distributions should be well described by only the zeroth and second Legendre polynomials, as appropriate for photoionization from an isotropic state. The measured angular distributions for a magic angle experiment with R_{21} (20.5) excitation are consistent with this prediction, as shown in Fig. 8. Note in particular the lack of nodes in the angular distributions of the $\Delta N = \pm 2$ peaks, which contrasts with those shown in Figs. 7, 9, and 12.

[1] J. Berkowitz, *Photoabsorption, Photoionization, and Photoelectron Spectroscopy* (Academic, New York, 1979).
[2] J. W. Rabalais, *Principles of Ultraviolet Photoelectron Spectroscopy* (Wiley, New York, 1977).
[3] D. Dill, in *Photoionization and Other Probes of Many-Electron Interactions*, edited by F. J. Wuilleumeir (Plenum, New York, 1975).
[4] J. L. Dehmer, J. Phys. Suppl. 7 **39**, C4-42 (1978).
[5] J. L. Dehmer, D. Dill, and A. C. Parr, in *Photophysics and Photochemistry in the Vacuum Ultraviolet*, edited by S. McGlynn, G. Findley, and R. Huebner (Reidel, Dordrecht, 1985).
[6] C. N. Yang, Phys. Rev. **74**, 764 (1948).
[7] J. Cooper and R. N. Zare, J. Chem. Phys. **48**, 942 (1968).
[8] For example, see S. T. Pratt, P. M. Dehmer, and J. L. Dehmer, in *Advances in Multi-photon Processes and Spectroscopy*, edited by S. H. Lin (World Scientific, Singapore, 1988), and the references and tabulation of REMPI-PES studies therein.
[9] K. Kimura, Int. Rev. Phys. Chem. **6**, 195 (1987).
[10] S. N. Dixit and V. McKoy, J. Chem. Phys. **82**, 3546 (1985).
[11] M. Sander, L. A. Chewter, K. Müller-Dethlefs, and E. W. Schlag, Phys. Rev. A **36**, 4543 (1987); K. Müller-Dethlefs, M. Sander, and E. W. Schlag, Z. Naturforsch. Teil A **39**, 1089 (1984); L. A. Chewter, M. Sander, K. Müller-Dethlefs, and E. W. Schlag, J. Chem. Phys. **86**, 4737 (1987); K. Müller-Dethlefs, M. Sander, and E. W. Schlag, Chem. Phys. Lett. **112**, 291 (1984).
[12] P. Kruit and F. H. Read, J. Phys. E **16**, 313 (1983).
[13] S. Edelstein, M. Lambropoulos, J. A. Duncanson, and R. S. Berry, Phys. Rev. A **9**, 2459 (1974).
[14] Y. Achiba, K. Sato, K. Shobatake, and K. Kimura, J. Chem. Phys. **78**, 5474 (1983).
[15] M. G. White, W. A. Chupka, M. Seaver, A. Woodward, and S. D. Colson, J. Chem. Phys. **80**, 678 (1984).
[16] Y. Achiba, K. Sato, and K. Kimura, J. Chem. Phys. **82**, 3959 (1985).
[17] S. T. Pratt, P. M. Dehmer, and J. L. Dehmer, J. Chem. Phys. **85**, 5535 (1986).
[18] K. S. Viswanathan, E. Sekreta, E. R. Davidson, and J. P. Reilly, J. Phys. Chem. **90**, 5078 (1986).
[19] For example, J. R. Appling, M. G. White, W. J. Kessler, R. Fernandez, and E. D. Poliakoff, J. Chem. Phys. **88**, 2300 (1988).
[20] H. S. Carman, Jr. and R. N. Compton, J. Chem. Phys. **90**, 1307 (1989).
[21] S. L. Anderson, G. D. Kubiak, and R. N. Zare, Chem. Phys. Lett. **105**, 22 (1984).
[22] S. T. Pratt, P. M. Dehmer, and J. L. Dehmer, J. Chem. Phys. **85**, 3379 (1986).
[23] P. J. Miller, W. A. Chupka, J. Winniczek, and M. G. White, J. Chem. Phys. **89**, 4058 (1988).
[24] W. G. Wilson, K. S. Viswanathan, E. Sekreta, and J. P. Reilly, J. Phys. Chem. **88**, 672 (1984).
[25] S. N. Dixit, D. L. Lynch, V. McKoy, and W. M. Huo, Phys. Rev. A **32**, 1267 (1985).
[26] H. Rudolph, S. N. Dixit, V. McKoy, and W. M. Huo, Chem. Phys. Lett. **137**, 521 (1987).
[27] H. Rudolph, S. N. Dixit, V. McKoy, and W. M. Huo, J. Chem. Phys. **88**, 637 (1988).
[28] H. Rudolph, S. N. Dixit, V. McKoy, and W. M. Huo, J. Chem. Phys. **88**, 1516 (1988).
[29] H. Rudolph and V. McKoy, J. Chem. Phys. **91**, 2235 (1989).
[30] S. L. Anderson, D. M. Rider, and R. N. Zare, Chem. Phys. Lett. **93**, 11 (1982).
[31] D. A. Dahl, *Simion PC/Ps2*, Idaho National Engineering Laboratory, EG&G Idaho, Inc., P. O. Box 1625, Idaho Falls, ID 83415.
[32] R. Englemen, P. E. Rouse, H. M. Peek, and V. D. Baiamonte, *Beta and Gamma Band System of Nitric Oxide* (Los Alamos Scientific Laboratory of the Univesity of California, Los Alamos, 1970).
[33] D. C. Jacobs, R. J. Madix, and R. N. Zare, J. Chem. Phys. **85**, 5469 (1986), see references therein.
[34] D. C. Jacobs and R. N. Zare, J. Chem. Phys. **85**, 5457 (1986).
[35] D. T. Biernacki, S. D. Colson, and E. E. Eyler, J. Chem. Phys. **89**, 2599 (1988).
[36] K. P. Huber and G. Herzberg, *Molecular Spectra and Molecular Structure IV. Constants of Diatomic Molecules* (Van Nostrand Reinhold, New York, 1979).
[37] K. S. Viswanathan, E. Sekreta, and J. P. Reilly, J. Phys. Chem. **90**, 5658 (1986).
[38] L. T. Earls, Phys. Rev. **48**, 423 (1935).
[39] R. N. Zare, *Angular Momentum* (Wiley, New York, 1988).

[40]For example, see G. Leuchs, in *Laser Physics*, edited by J. D. Harvey and D. F. Walls, Lecture Notes in Physics Vol. 182 (Springer, Berlin, 1983).
[41]H. Rudolph, V. McKoy, and S. N. Dixit, J. Chem. Phys. **90**, 2570 (1989).
[42]S. N. Dixit and V. McKoy, Chem. Phys. Lett. **128**, 49 (1986).
[43]For a complete listing of the partial wave decomposition, see S. W. Allendorf, Ph.D. Dissertation, Stanford University, Stanford, California, 1989.
[44]S. Dixit and P. Lambropoulos, Phys. Rev. A **27**, 861 (1983).
[45]D. Dill, Phys. Rev. A **6**, 160 (1972).
[46]U. Fano and D. Dill, Phys. Rev. A **6**, 185 (1972).
[47]W. H. Press, B. P. Flannery, S. A. Teukolsky, and W. T. Vetterling, *Numerical Recipes* (Cambridge University, Cambridge, 1986).